3. New perspectives on the Bishop Tuff from zircon textures, ages and trace elements

This is a pre-copyedited, author-produced version of an article accepted for publication in Journal of Petrology following peer review. The version of record is available online at: https://doi.org/10.1093/petrology/egt072

Abstract

We present zircon textural, trace element and U–Pb age data obtained by secondary ion mass spectrometry (SIMS) (SHRIMP-RG: sensitive high resolution ion microprobe- reverse geometry) from 15 stratigraphically controlled Bishop Tuff samples and 2 Glass Mountain (GM) lava samples (domes OD and YA). Bishop zircon textures divide into four suites, (a) dominant sector-zoned grains, with (b) subordinate grains showing bright rims (lower U, Th, rare earth elements [REE]) in CL imaging, and sparse (c) GM-type grains (texturally similar to zircons from GM dome YA) and (d) Mesozoic xenocrysts from Sierran granitoid country rocks. All Bishop zircons from suites (a) – (c) combined have a weighted mean age of 777.9 ± 2.2 ka (95% confidence) and a tail back to ~845 ka. Our eruption age estimate using the weighted mean of 166 rim ages of 766.6 ± 3.1 ka (95% confidence) is identical within uncertainty to published estimates from isotope-dilution thermal ionization mass spectrometry (ID-TIMS) (767.1 ± 0.9 ka, 2σ) and $^{40}Ar/^{39}Ar$ (767.4 ± 2.2 ka, 2σ) techniques, the latter using the 28.172 Ma age for the Fish Canyon sanidine standard. We estimate also an eruption age for GM dome YA of 862 ± 23 ka (95% confidence), significantly older than the currently accepted 790 ± 20 ka K-Ar age. The oldest zircon cores from late-erupted Bishop material (including those with GM-type textures) have a weighted mean of 838.5 ± 8.8 ka (95% confidence), implying that the Bishop Tuff system was only active for ~80 kyr, and had effectively no temporal overlap with the GM system. Trace element variations in Bishop zircons are influenced strongly for many elements by sector zoning, producing up to 3x concentration differences between sides and tips within the same growth zones. Contrasting trends in molar $(Sc+Y+REE^{3+})/P$ ratios between sides and tips indicate contrasting mechanisms of substitution in different sectors of the same crystal. Concentrations of Ti in tips are double those in the sides of crystals, hindering applicability of the Ti-in-zircon thermometer, in addition to variations inherent to the 0.15 – 0.67 range in values proposed for $a TiO_2$. The bright-rim portions of grains are inferred to have crystallized from the same magma as generated the bright rims seen under cathodoluminescence or back-scattered electron imaging on quartz and feldspar, respectively. This less evolved, slightly hotter magma

invaded the deeper parts of the chamber represented in the late-erupted northern units possibly up to ~10 kyr prior to eruption, but only invaded shallower levels very shortly before eruption as shown by our textural information and previously proposed from the sharp delineation of quartz bright rims. By obtaining a large number of analyses from zircon separates which systematically cover the entire Bishop Tuff eruption sequence we can produce an eruption age estimate using SIMS to the same precision and accuracy as ID-TIMS and $^{40}Ar/^{39}Ar$ techniques.

3.1. Introduction

The Bishop Tuff has become an iconic representative of the largest group of felsic explosive volcanic eruptions ('supereruptions') and a central focus of debates on the origin, assembly and compositional zonation of large silicic magma bodies. In particular, following the seminal studies of Hildreth (1977, 1979) and their setting into regional and global perspectives (Hildreth, 1981, 2004), several key areas have remained controversial. The central inference of Hildreth (1977, 1979) of a pre-eruptive, vertically and laterally continuous >600 km^3 body of moderate- to high-silica rhyolite, vertically zoned with respect to composition (particularly trace elements), crystal and volatile contents, and temperature has remained (Dunbar & Hervig, 1992a; Wallace *et al.*, 1999; Anderson *et al.*, 2000; Bindeman & Valley, 2002; Hildreth & Wilson, 2007; Roberge *et al.*, 2013, but see also Gualda *et al.*, 2012a).

There remains vigorous debate, however, about two aspects of this picture which we consider here from the zircon perspective. The first concerns inconsistencies between estimates of the eruption age derived from $^{40}Ar/^{39}Ar$ experiments on sanidine, and between those estimates and values derived from U–Pb dating of zircons using high-precision ID-TIMS methods. The second concerns the longevity of the Bishop magma chamber, the timing of its assembly and the magmatic regime, derived from various lines of evidence and modelling. To address these issues, we present a comprehensive suite of zircon age determinations and associated trace element data obtained by secondary ion mass spectrometry (SIMS). We have analyzed zircons from fifteen stratigraphic horizons in the Bishop Tuff in order to trace the geochronological and trace-element development of the magma chamber as recorded in discrete zones of single crystals. Although single SIMS age determinations are less precise than those derived from single-zircon ID-TIMS techniques, the ability to create large data sets from discrete zones in single zircons from different

pumice types and different eruptive units within the Bishop Tuff places powerful constraints on the pre-eruptive history of the magma body. Additionally, collection of trace-element data and the linkage to zircon textures as shown in cathodoluminescence (CL) imaging allow the overall petrogenetic context and broad timings of interaction of the zircon crystals with different magma compositions to be assessed.

3.2. The Bishop Tuff

3.2.1. Geological background

The >600 km^3 Bishop Tuff was erupted in association with formation of Long Valley caldera in eastern California (Fig. 3.1; Bailey *et al.*, 1976; Hildreth, 1979, 2004; Wilson & Hildreth, 1997; Hildreth & Wilson, 2007). The eruption represented the culmination of ~4.5 Myr of magmatism and the rhyolite erupted in the Bishop Tuff event is greater in volume than all other felsic eruptions combined in the Long Valley area before or since (Hildreth, 2004).

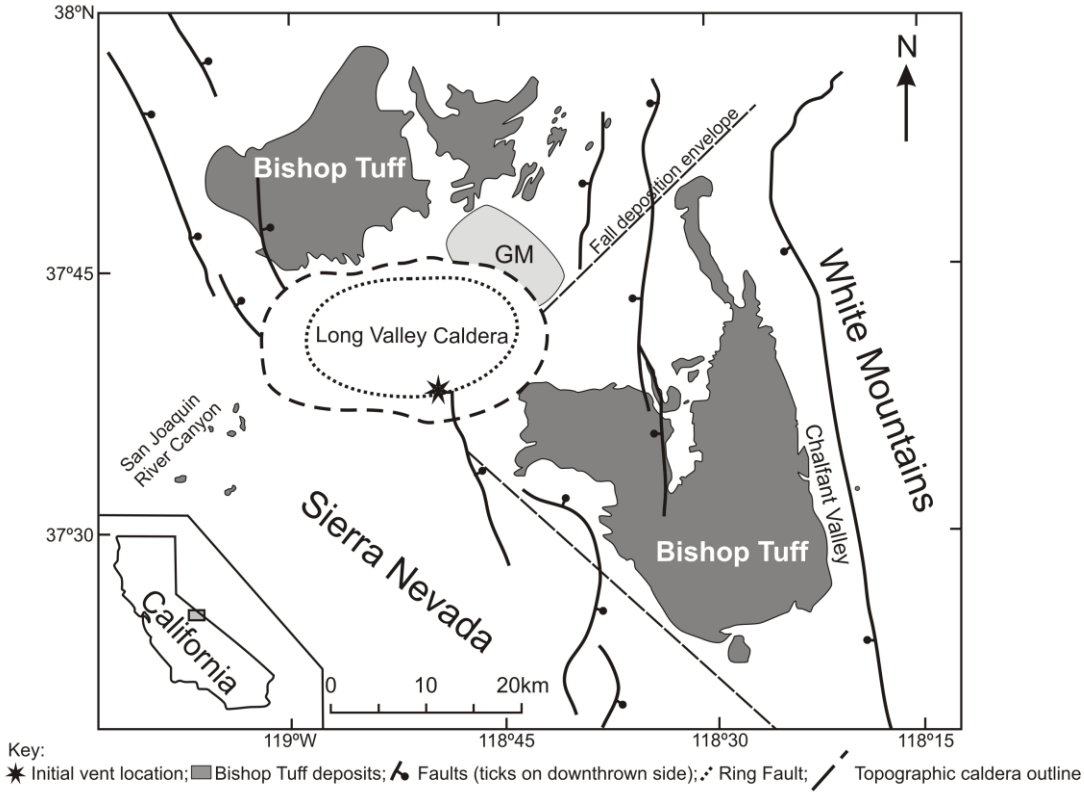

Fig. 3.1. Map of the Long Valley area, eastern California, USA, after Hildreth & Wilson (2007). The topographic outline of the caldera is shown as a dashed line, with the ring-fault zone shown as a dotted ellipse inside the topographic margin. Regions of Bishop pyroclastic-flow deposition are shaded grey. The envelope enclosing precursory Glass Mountain (GM) lava domes is highlighted in light grey. The line marked 'Fall deposition envelope' marks the westerly limits of where Bishop fall deposits are found in this area.

The Bishop Tuff in its proximal outcrop area between the Sierra Nevada and White Mountains (Fig. 3.1) consists of a sequence of plinian pumice fall deposits generated before, and coevally with, lobes of ignimbrite, together with voluminous co-eruptive caldera fill (Wilson & Hildreth, 1997). In these proximal areas where we (and all other workers concerned with pumice in the Bishop Tuff) have sampled, the fall deposits are found only in an ~90° sector east of source; however the overall blanket of fall deposits (plinian and co-ignimbrite) covers much of the western USA to >2000 km from source (Izett *et al.*, 1988). Marker horizons in the proximal fall deposits were used to divide them into nine units (F1 to F9). In turn, interbedding relationships and recognition of other marker horizons were used to correlate between the fall and flow deposits and estimate that the eruption occurred (with only one possible very short hiatus between F8 and F9) over a period of the order of 6 days (Wilson & Hildreth, 1997).

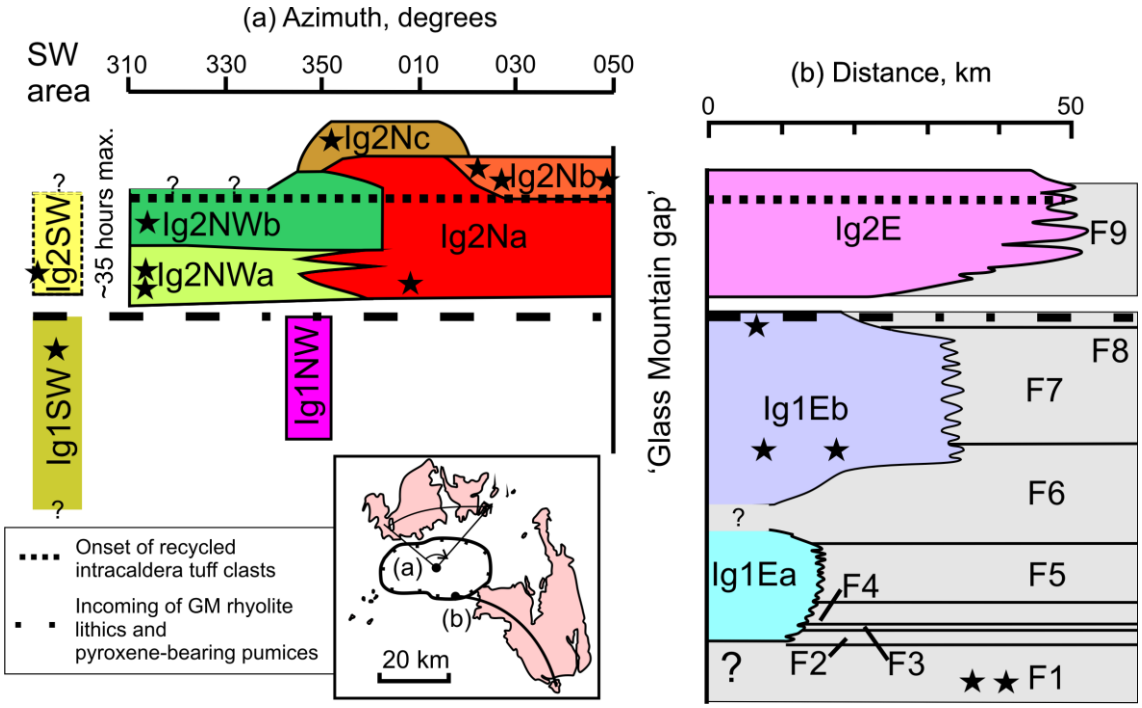

Fig. 3.2. Summary stratigraphy of the Bishop Tuff, after Hildreth & Wilson (2007). Locations for samples in this study are starred (see Table 3.1 for sample numbers and sites). (a) Hypothetical cross section from NW to NE across the northern ignimbrite lobes as viewed from the centre of Long Valley caldera. (b) Schematic proximal to distal cross-section approximately along the line of Owens River Gorge, where the horizontal axis represents distance from the initial vent site of Hildreth & Mahood (1986). Enlarged stratigraphy figure is also repeated in Appendix 1.

Lithic assemblages in the fall deposits and ignimbrite serve to locate the initial vent in the southeastern sector of what became the caldera and then follow the subsequent concurrent development of venting along the northern and eastern portions of the ring fracture (Figs. 3.1, 3.2: Hildreth & Mahood, 1986; Wilson & Hildreth, 1997).

Prior to the Bishop Tuff eruption the Glass Mountain rhyolitic system was active from 2.2 Ma to 790 ka, producing more than 60 effusive and explosive eruptions, and building a lava dome complex with a surrounding fan of primary and reworked volcaniclastic material (Metz & Mahood, 1985, 1991; Metz & Bailey, 1993; Hildreth, 2004). This system has two sub-groups: a 2.2 – 1.3 Ma sequence of chemically variable, exceedingly evolved high-silica rhyolites, and a younger group (1.2 Ma to 790 ka) of chemically more uniform, highly evolved high-silica rhyolites, the latter similar in bulk composition to the early Bishop eruption products (Metz & Mahood, 1991; Hildreth, 2004). Glass Mountain rhyolites are dominantly crystal poor (<8% crystals), with similar mineral assemblages to the Bishop Tuff (Metz & Mahood, 1991). Earlier rhyolitic volcanism is represented by plinian pumice fall deposits, best exposed in the Blind Spring Valley area east of Glass Mountain but which also extend for hundreds of kilometres farther east (Sarna-Wojcicki *et al.*, 2005). Younger parts of this sequence were correlated with Glass Mountain activity, but older lapilli-bearing (hence probably within tens of kilometres of vent) fall deposits returned $^{40}Ar/^{39}Ar$ single-crystal sanidine ages of between *c.* 2.2 and 2.8 Ma (Sarna-Wojcicki *et al.*, 2005). As such, these deposits apparently pre-date activity at the Glass Mountain system and came from sources as yet undefined within the Long Valley area.

3.2.1. Eruption age estimates

The age of the Bishop Tuff has long been of interest globally because of its proximity in time to the Matuyama Reversed to Brunhes Normal (M–B) paleomagnetic transition (e.g. Sarna-Wojcicki *et al.*, 2000; Mark *et al.*, 2012; Singer *et al.*, 2012). Two contrasting approaches have been used to assess the Bishop Tuff eruption age: U–Pb geochronology, both by ID-TIMS and SIMS techniques, and Ar–Ar geochronology.

Crowley *et al.* (2007) reported high-precision ID-TIMS U–Pb age determinations on a suite of zircons from a densely welded zone of Bishop Tuff in the Owens River gorge. From their description we infer their sample to be from the dense-welded portion of Ig1Eb (welding zone c of Wilson & Hildreth, 2003; Fig 3.2b). The zircons illustrated in Crowley

et al. (2007) are dominated by a sector-zoned structure, often with an apparent central domain and U concentrations ranging from under 1000 ppm to 2000 ppm in the central domain to over 5000 ppm in pyramidal tips. These zircons yielded a weighted mean estimate of 767.1 ± 0.9 ka [2σ, mean square of weighted deviates (MSWD) = 1.3] from 17 of 19 grains analysed.

U–Pb age determinations by SIMS have been reported by Reid & Coath (2000), Simon & Reid (2005) and Reid & Schmitt (2012). The ion microprobe uses a focused ion beam to sputter the target with the advantage of allowing selection of particular domains in the zircon. However, the fine sampling scale of the ion microprobe greatly diminishes the sample size and there is a commensurate loss of precision. However, the issue of ion microprobe analysis is not simply the final determination of a bulk age, but rather the association of that age with discrete structures in the zircon. Reid & Coath (2000) and Simon & Reid (2005) determined that zones in the zircons showed a significant pre-eruptive history extending back hundreds of thousands of years. Although such prehistory should have also been apparent in the bulk ID-TIMS analyses, the samples analyzed were not the same and the possibility arises that there could be stratigraphic variations in the zircon age characteristics. Simon & Reid (2005) reported weighted mean crystallisation ages (uncertainties reported as 1 σ_m) of 811 ± 7 ka (MSWD = 3.4, 20 analyses on 14 grains) for interiors of grains from Ig2NW[b], 841 ± 8 ka (MSWD = 0.9, n = 29) from rims of grains from Ig1Eb, and 823 ± 14 ka (MSWD = 0.8, 22 analyses on 20 grains) from Ig1Eb [also reported by Reid & Coath (2000)]. Pooled minimum ages (i.e. first-order estimates of eruption age) from the first two of these data sets were given as 753 ± 11 ka (n = 7) and 767 ± 30 ka (n = 4), respectively.

Closely similar eruption-age estimates to those from U–Pb experiments were obtained from 20–25 grain multi-crystal total fusion $^{40}Ar/^{39}Ar$ experiments on Bishop sanidines by Rivera *et al.* (2011) from the same sample (79G94) as used by Sarna-Wojcicki *et al.* (2000). From their descriptions, we infer this sample to be from ignimbrite packages Ig2Na or Ig2Nb of Wilson & Hildreth (1997). Rivera *et al.* (2011) derived a weighted mean for the Bishop sanidines of 767.4 ± 2.2 ka (2σ, external errors), along with an equivalent astronomically intercalibrated $^{40}Ar/^{39}Ar$ age for the Fish Canyon Tuff (FCT) sanidine standard (FCT) of 28.172 ± 0.028 Ma (2σ, external errors).

The apparently excellent agreement between U–Pb age determinations and $^{40}Ar/^{39}Ar$ experiments conflicts, however, with proposals for contrasting values for the ^{40}K decay constant and consequent FCT standard age values that would have the Bishop Tuff eruption age being significantly older (Renne *et al.*, 2010, 2011; Mark *et al.*, 2012). The eruption age estimate derived from the experiments of Sarna-Wojcicki *et al.* (2000) would shift to 778.4 ± 3.7 ka [2σ, using the 28.305 ± 0.036 Ma FCT age from Renne *et al.* (2010)] or 778.1 ± 3.7 ka [2σ, after Renne *et al.* (2011): FCT age of 28.294 ± 0.036 Ma]. Further age determinations by Mark *et al.* (2012) on the same feldspar sample as used by Sarna-Wojcicki *et al.* (2000) and Rivera *et al.* (2011) were reported as 776.4 ± 0.9 ka (inferred by us to be 1σ), on the basis of the Renne *et al.* (2011) FCT value.

3.2.3. Magma accumulation timescales

A range of methods have been used to investigate timescales of magma accumulation and residence in silicic systems [for reviews see Hawkesworth *et al.* (2000, 2004)]. It should be noted, however, that the term 'residence time' may be interpreted in different ways. A distinction is drawn by us between the lifetimes of crystals (reflecting complex, possibly prolonged patterns of growth, stasis or dissolution) and the lifetime of the melt-dominant body in which they were suspended when quenched on eruption. Hildreth (1979) proposed that the crystal population in Bishop pumices grew *in situ* and that the species present reflected the overall zonation in bulk-compositional characteristics. On this basis, the age range of the crystals and the lifetime of the melt-dominant body should be effectively the same. In contrast, studies of comparably-sized systems (Bindeman *et al.*, 2001; Charlier *et al.*, 2005, 2008, 2010) show that crystal populations in deposits pre- and post-dating the climactic events are influenced by inheritance and recycling of antecrysts (from earlier crystallization events in the system) and xenocrysts (from local basement rocks). The age spectra of zircons within the Oruanui (New Zealand) pumices demonstrably bear no resemblance to the much shorter timescale for growth of the final melt-dominant body that was evacuated in the Oruanui eruption (Wilson & Charlier, 2009; Allan *et al.*, 2013).

For the Bishop Tuff, at one extreme, timescales of the order of hundreds of thousands to a million years have been proposed for development of the parental magma body. Glass-feldspar Rb/Sr isochrons from Glass Mountain lavas (particularly those from ~1.1 Ma onwards), and pumices from the Bishop Tuff itself, yield model ages 300 to 1300 kyr older than notional eruption ages (Halliday *et al.*, 1989; Christensen & DePaolo, 1993;

Christensen & Halliday, 1996; Davies & Halliday, 1998). This protracted timescale was apparently supported by $^{40}Ar/^{39}Ar$ ages from melt inclusions in quartz (2.0 – 2.3 Ma; van den Bogaard & Schirnick, 1995), but these ages were subsequently attributed to excess Ar (Winick *et al.*, 2001). Theoretical models of felsic magma genesis have also been used to estimate a million year timescale for development of the Bishop magma (Fowler & Spera, 2010), but this approach has been suggested to be unrealistic on the grounds of thermal constraints (Gualda & Ghiorso, 2011; Fowler & Spera, 2011).

Studies focusing on the chronological information from zircons have, however, yielded shorter and contrasting timescales. Zircon in the Bishop Tuff is considered to be one of the earliest crystallising phases (Hildreth, 1979) on the basis of its presence as inclusions within all other crystal species. It would thus be expected that the zircon age spectra should date the timescales of crystallization during generation of the Bishop magma in the overall crystal-dominated roots of the magmatic system (the mush zone: Bachmann & Bergantz, 2004; Hildreth, 2004). There is, however, a distinct contrast between zircon mean ages of 811 – 841 ka plus the ~160 kyr range of pre-eruptive ages from SIMS (Reid & Coath, 2000; Simon & Reid, 2005; Reid *et al.*, 2011) and the ~12 kyr maximum range proposed from ID-TIMS (Crowley *et al.*, 2007). This contrast has been further highlighted by proposals (Gualda *et al.*, 2012a,b; Pamukcu *et al.*, 2012) that crystallisation histories of the major mineral phases in the Bishop magma occurred over a much smaller range in magmatic temperatures (757 – 762 °C: Gualda *et al.*, 2012a) than those inferred from Fe-Ti oxide equilibria (714 – 818 °C: Hildreth & Wilson, 2007) and over associated shorter timescales, more consistent with those implied by the results of Crowley *et al.* (2007).

3.2.4. Trace element patterns

The great variations in trace-element abundances within the Bishop pumices were first highlighted by Hildreth (1977, 1979) and attributed to liquid-state fractionation (Soret diffusion). This specific mechanism has since been demonstrated to be inappropriate (Lesher, 1986), and the variations are now considered to result from crystal fractionation processes (Michael, 1983; Cameron, 1984) in the mush zone, with extraction of variably fractionated liquids to form the melt-dominant body (Hildreth, 2004; Hildreth & Wilson, 2007) although debate still remains. The crystal-specific record shows, however, further complexities. The outer zones of crystals (together with their melt inclusions) from pumices in ignimbrite lobes north and northwest of the caldera rim show contrasting

textures that correlate with trace-element patterns. Many quartz, sanidine and zircon crystals from these inferred later-erupted materials have outer zones that are brighter under cathodoluminescence (CL) (quartz, zircon) or back-scattered electron (BSE) imaging (sanidine), and have volatile abundances and trace-element patterns indicative of crystallisation from a less-evolved, inferred hotter melt (Dunbar & Hervig, 1992a; Wallace *et al.*, 1999; Anderson *et al.*, 2000; Peppard *et al.*, 2001; Wark *et al.*, 2007; Reid *et al.*, 2011). Originally interpreted to reflect sinking of the crystals from the 'normal' Bishop magma (represented by the earlier-erupted plinian fall deposits and eastern-side ignimbrite lobes) into the contrasting magma (Wallace *et al.*, 1999; Anderson *et al.*, 2000; Peppard *et al.*, 2001), these features are now interpreted to reflect ingress into the Bishop chamber of the contrasting magma type (e.g. Wark *et al.*, 2007; Reid *et al.*, 2011). The boundaries between the 'normal' (i.e., crystals typical of earlier-erupted plinian fall deposits and eastern-side ignimbrite) cores and contrasting rims in the crystals are often sharp to <10 μm. Such abrupt changes have been linked to introduction of a contrasting magma that may have triggered the onset of the eruption itself (e.g. Wark *et al.*, 2007; Reid *et al.*, 2011), and/or accompanied rapid rise of the host magma to shallow depths (Thomas *et al.*, 2010; cf. Wilson *et al.*, 2012).

Trace-element patterns within Bishop zircons from 'early' versus 'late'-erupted material show wide variations (Hildreth, 1979; Mahood & Hildreth, 1983 from bulk crystal aliquots; Reid *et al.*, 2011 from single crystals) that match closely the variations seen in the quartz and feldspar. As shown by Reid *et al.* (2011) and amplified in this study, however, most of the trace element contrasts arise from variations within the individual crystals. Outer rims, brighter under CL imaging, occur on virtually no grains in the early erupted material, but are frequent and up to tens of microns thick on grains from the late-erupted material. Melt compositions indicated by the bright-rim material or represented by melt inclusions in these rims, were inferred or demonstrated to represent less-evolved and/or hotter melts (Wallace *et al.*, 1999; Anderson *et al.*, 2000; Wark *et al.*, 2007). However, our work shows that this picture is neither as simple, nor as uniform as implied by these earlier studies.

3.2.5 Sample suites for this study

Fifteen samples of the Bishop Tuff were selected for zircon extraction (Table 3.1; Fig. 3.2), plus two samples from Glass Mountain domes OD (K-Ar age of 1.33 ± 0.01 Ma) and YA (0.79 ± 0.01 Ma) (ages from Metz & Mahood, 1985). The tuff was systematically sampled

by us from the earliest fall unit (F1) through to the latest ignimbrite unit (Ig2Nc) to track any vertical and lateral variations present within the single zoned magma body. A range of pumice types was selected, from crystal-poor to crystal-rich in the 'normal' pumice spectrum as well as some of the 'variant' very crystal-poor pumices (Hildreth & Wilson, 2007; see Table 3.1 for brief sample descriptions).

Table 3.1. Samples used in this study

Sample Number	Unit	Type	Location	Grid Ref	Brief Description
BP109	F1	multi	Owens River Gorge	03594, 41564	Bottom 12cm bulk sample of F1 (pumices sieved to > 1 mm).
BP178	F1	multi	Owens River Gorge	03550, 41607	Bulk pumice sample of 2.8-8 mm fraction from F1.
BP087	Ig1Eb	xp	Owens River Gorge	03594, 41564	Very fresh, large (26 cm) pumice crystal -poor to -moderate.
BP098	Ig1Eb	vxp-sw	Owens River Gorge	03594, 41564	Moderately vesicular vxp pumice with a sugary texture- swirly type.
BP130	Ig1SW	multi	Sotcher Lake	03174, 41661	Bulk sample of the largest single unoxidised pumices.
BP040	Ig1Eb (Sherwin)	xr	Sherwin Grade	03483, 41578	Oxidised, crystal rich, 'Adobe' type single pumice.
BP216	Ig2SW	multi	Pumice Butte	03169, 41572	Bulk sample of largest single pumice clasts from the upper parts of Ig2SW.
BP118	Ig2NWa	xr	Crestview	03241, 41812	Moderately vesicular crystal-rich pumice with a uniaxial fibrous texture.
BP115	Ig2NWa	vxr	Crestview	03241, 41812	Moderately vesicular very crystal-rich pumice with a planar fabric.
BP059	Ig2Na	xr	Bald Mountain Spring	03381, 41879	Fresh, moderately vesicular, very crystal-rich single pumice.
BP124	Ig2NWb	xr	Aeolian Buttes	03175, 41925	Moderately vesicular crystal-rich single clast with a fibrous texture.
BP170	Ig2Nb	xr	McGee Lobe	03477, 41871	Core of a very fresh crystal-rich pumice with a crimped-fibrous texture.
BP172	Ig2Nb	xp-sw	McGee Lobe	03477, 41871	Very crystal-poor, moderately vesicular light grey swirly pumice.
BP232	Ig2Nb	xp-sw	McGee Lobe	03476, 41872	Pale grey, finely vesicular pumice with a foamy texture- swirly.
BP206	Ig2Nc	xr	Granite Mountain	03422, 41971	Crystal-rich single clast with an Adobe-like texture.
BR228	Dome YA	xp lava	Dome YA-Glass Mountain	03409, 41846	Very crystal-poor obsidian.
BR226	Dome OD	xm	Dome OD-Glass Mountain	03449, 41877	Crystal-moderate to -rich lava.

Erupted units and types are from Hildreth & Wilson (2007). For pumice type descriptions see Table 2.1 in Chapter 2.

Fourteen samples are from single pumice clasts (Bishop) or obsidian dome carapace material (Glass Mountain). For Bishop Ig1SW and Ig2SW samples, due to a lack of pumices of adequate size, zircons were extracted from multiple lapilli-sized pumices. For the samples from fall F1, bulk samples were taken, sieved (to exclude free crystals) and a pumice fraction separated by water panning and hand-picked (to remove lithic fragments) before crushing for zircon extraction.

3.3. Analytical techniques

Zircon crystals for analysis were handpicked from a 60 – 250 μm sieve fraction pumice crush, which had been concentrated using standard density and magnetic separation techniques. Age determinations were made by SIMS techniques on the SHRIMP-RG instruments at the joint USGS-Stanford University facility (SUMAC) and at the Research School of Earth Sciences, Australian National University (ANU). Zircons were mounted in epoxy resin, polished to expose the cores of the grains, and imaged in reflected light, transmitted light, as well as by CL on a scanning electron microprobe (SEM) at SUMAC and ANU. To minimise contamination by common Pb, the mounts were cleaned in detergent, petroleum spirits or dilute EDTA, and 1 M HCl, with intervening rinses in distilled water, then gold coated.

During analysis, the primary beam was rastered for 180 seconds over an area of 35 x 45 μm prior to data acquisition to remove the gold coat and any possible surface contamination. Secondary ions were then sputtered with a 5-6 nA primary O_2^- beam focused to a ~25 x 35 μm spot. The mass spectrometer was cycled through peaks corresponding to (bracketed species run at SUMAC only) ($^{172}Yb^{16}O$), $^{90}Zr_2{}^{16}O$, ($^{180}Hf^{16}O$), ^{204}Pb, background, ^{206}Pb, ^{207}Pb, ^{208}Pb, (^{232}Th), ^{238}U, $^{232}Th^{16}O$ and $^{238}U^{16}O$, with a total analysis time of 750 – 900 s. Extended count times were used for ^{206}Pb (20 or 30 s) and ^{207}Pb (20 s) and six scans were run through the mass sequence. The concentration standard was MAD (Madagascar green: Barth & Wooden, 2010; 4196 ppm U) at SUMAC and SL13 (238 ppm U) at ANU. The U–Pb age standard throughout was R33 (420 Ma: ID-TIMS age from: http://earth.boisestate.edu/isotope/analytical-capabilities/id-tims-u-pb). Data reduction used SQUID 2 (Version 1.51: Ludwig, 2009), and data were plotted using Isoplot 3.76 (Ludwig, 2008). For single analyses uncertainties given by SQUID2 are reported here at 2σ, whereas for our grouped data sets uncertainties are given at the 95% confidence interval as

generated in Isoplot. In these grouped data sets weighted means are calculated using the 'reject OK?' option engaged in Isoplot.

The ^{230}Th correction for initial disequilibrium was calculated using the measured Th and U concentrations in the zircons from the SIMS measurements, together with melt Th/U values derived from laser ICP-MS data from glass separates for the Bishop Tuff samples (see Electronic Appendix 12) and published instrumental neutron activation analysis (INAA) data for the two Glass Mountain samples (Metz & Mahood, 1991). For comparison, Crowley *et al.* (2007) used a single value of 2.81 from the mean of 12 melt inclusion analyses published by Anderson *et al.* (2000). A correction factor was then applied using $f = (Th/U_{zir})/ (Th/ U_{wr})$, following Schärer (1984). The presence of common Pb was evaluated by monitoring ^{204}Pb and ^{207}Pb/^{206}Pb, and a correction was then applied using the recorded ^{207}Pb/^{206}Pb values and a common-Pb isotopic composition for the sample age from the average crust model of Stacey & Kramers (1975). This approach was tested using a regression of ^{238}U/^{206}Pb vs. ^{207}Pb/^{206}Pb for twenty spots with >20% of the ^{206}Pb attributable to common-Pb. This plot yielded a ^{207}Pb/^{206}Pb intercept of 0.82 ± 0.03, consistent with use of the Stacey & Kramers (1975) value for the sample age (see Electronic Appendix 1). Analyses of grains with >10% common Pb at U >500 ppm were excluded from the data set. However, some zircons from later-erupted pumices showed CL-bright zones which had <500 ppm U and accompanying higher proportions of common-Pb. For these 31 analyses a cut-off of 30% common-Pb was used and these data were handled separately.

SIMS analyses for trace elements were performed on the SHRIMP-RG at SUMAC using a 1.5–3 nA primary beam current and a focused 15 x 12 μm spot. Analytical sites were selected in order to avoid inclusions visible in reflected light images and to representatively sample different CL zones, as well as crystal cores and rims. Trace element analytical spots were not superimposed on the U–Pb age dating spots (and vice versa) , but care was taken to locate trace element analyses within the same growth zones of the zircon crystals as those that were age dated. The MAD zircon standard was used to calibrate trace element concentrations (Electronic Appendix 1).

3.4. Results

Our data suite consists of three quantifiable aspects of zircons: the textures as shown under CL imaging, the age data, and the trace-element data, which we first consider as separate entities.

3.4.1. Zircon textures

A total of ~3300 zircon crystals from the Bishop Tuff and Glass Mountain samples were characterised for their respective CL zoning patterns. When mounting the crystals, care was taken to lay prismatic crystals flat so that when they were ground down and polished, a representative cross section was made of textures in the plane of the *a*- and *c*- or *b*- and *c*-axes. The patterns observed are grouped into four main suites (Figs. 3.3, 3.4; Table 3.2) as follows:

(a) The 'typical' Bishop suite (referred to hereafter as 'normal Bishop') of euhedral prismatic grains, almost always with a strongly developed sector-zonation but lacking bright rims (Fig. 3.3a-c). This type overwhelmingly dominates the zircon populations from the fall deposit and easterly-distributed ignimbrite, and is still present in all samples from the northern ignimbrite lobes. All the grains illustrated by Crowley *et al.* (2007) belong to this type.

(b) A subordinate suite having some proportion of the crystal that displays distinctly bright CL shades when compared to the normal Bishop type, and labelled 'bright rim' type (Fig. 3.3c-e). The bright material most often forms discrete, sharply defined rims on grains, the cores of which have morphologies and CL patterns similar to the normal Bishop grains (above), but also comprises whole grains or continuously CL-zoned grains in samples from some of the northern lobes. The zircons with bright rims were further separated into four categories: <10 μm rim; 10 – 30 μm rim; rim >30 μm wide overgrowing a core of contrasting composition; >80% of the crystal showing bright CL shades and inferred to have largely or wholly crystallised from the 'bright-rim magma'.

(c) A sparsely developed suite of oscillatory zoned, poorly shaped crystals with little or no visible indications of sector zoning (Fig. 3.3f). This type comprises virtually all of the grains for the YA dome sample (Fig. 3.4) and is thus termed 'Glass Mountain type'. Grains with similar characteristics are a sparse (0 – 6%) component of the zircon suites in pumices from northern and northwestern Bishop ignimbrite lobes.

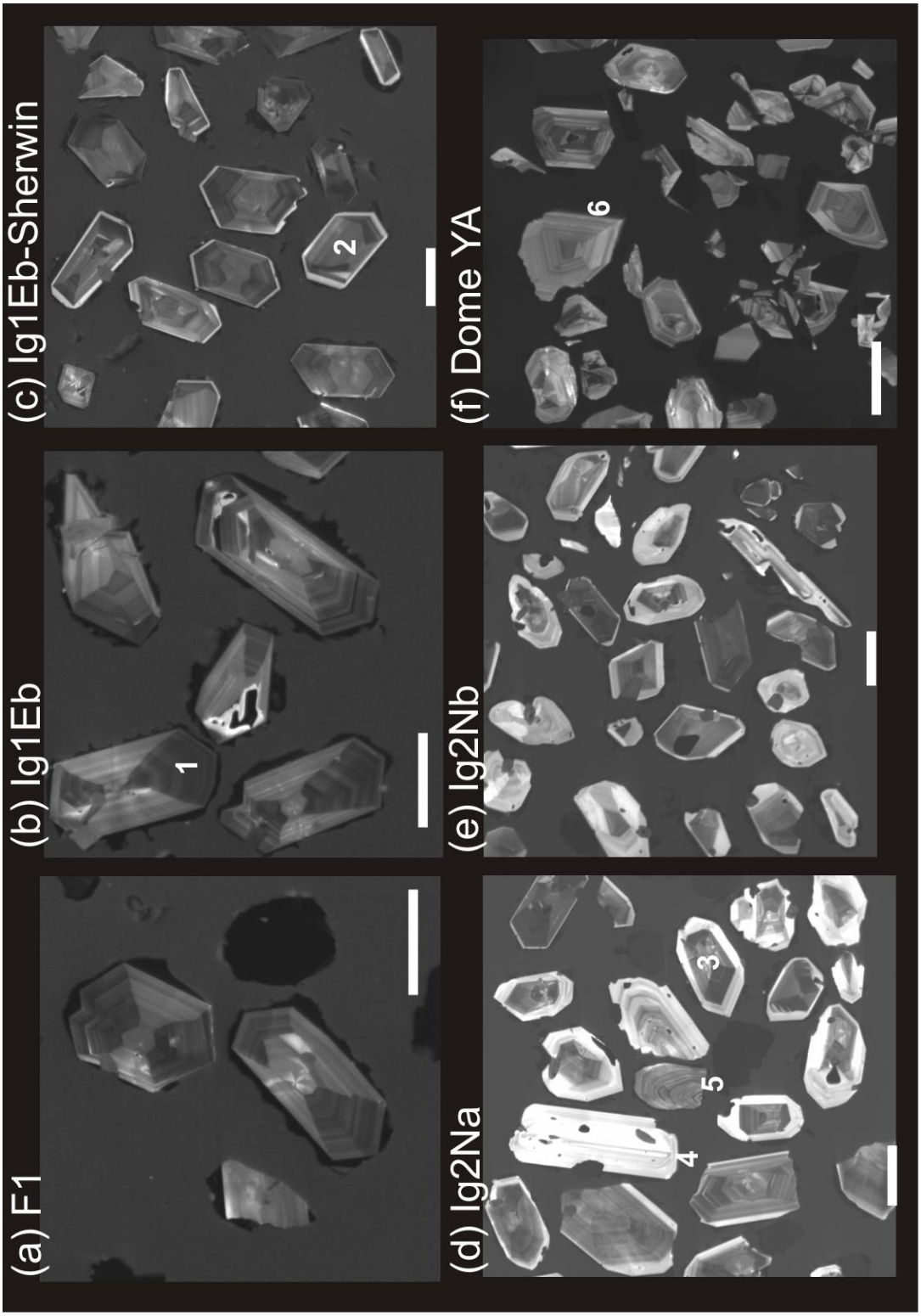

Fig. 3.3. Zircon CL textures shown in samples from the Bishop Tuff (a–e) compared with those of the youngest Glass Mountain (GM) dome [YA (f): see text for details]. (a) BP178-F1; (b) BP087-Ig1Eb; (c) BP040-Ig1Eb- Sherwin; (d) BP059-Ig2Na; (e) BP170-Ig2Nb (See Table 3.1 for sample descriptions). Types of zircons described in the text are as follows: 1, dominantly sector-zoned 'normal Bishop' zircons showing the characteristic oscillatory zoning; 2, 'normal Bishop'-type zircon with a narrow (<10 μm) bright rim; 3, a wide bright rim overgrowing a 'normal Bishop'-type zircon; 4, a completely CL-bright zircon; 5, Triassic zircon showing oscillatory zoning with no sector-zoning or bright rim: the crystal is fractured but still glass coated; 6, Glass Mountain-type oscillatory zoned crystal. Scale bar represents 100 μm in each image.

(d) A sparsely developed suite of concentrically zoned irregularly shaped to euhedral grains which are commonly fractured, oscillatory zoned, and darker in CL than the Glass Mountain type (Fig. 3.3d, labelled as grain 5). Trace-element analyses, incorporating short counts for ^{206}Pb (10 seconds) and $^{238}U^{16}O$ (5 seconds) for Pb and U concentrations, respectively, showed that such grains are xenocrystic (although glass coated, showing that they are not accidental), returning Mesozoic, overwhelmingly Triassic, ages inferred to reflect a source in the local Sierra Nevada granites (Barth *et al.*, 2011). These grains are labelled as 'basement type' hereafter.

Systematic changes in zircon textures are observed in pumices collected through the Bishop Tuff eruptive sequence (Fig. 3.4; Electronic Appendix 2).

Table 3.2. Summary of textural features observed in zircons from Bishop Tuff samples examined in this study

Sample	Eruptive unit	Number of grains	Sector zoned, %	No bright rim, %	<10 µm bright rim, %	10-30 µm bright rim, %	>30 µm bright rim, %	All bright %	Mesozoic, %	Glass Mtn, %
BP206	Ig2Nc	688	24	5	32	27	8	22	3	3
BP124	Ig2NWb	257	23	1	31	33	14	16	2	3
BP172	Ig2Nb	67	42	43	9	9	6	15	18	0
BP232	Ig2Nb	190	44	41	13	7	5	7	21	6
BP170	Ig2Nb	53	15	0	11	51	21	13	0	4
BP059	Ig2Na	257	61	3	32	30	16	14	3	4
BP115	Ig2NWa	624	32	1	30	33	14	20	2	1
BP118	Ig2NWa	98	89	4	67	22	3	3	0	0
BP216	Ig2SW	306	67	42	54	2	0	1	1	0
BP040	Ig1Eb (Sherwin)	239	86	31	58	10	0	1	0	0
BP130	Ig1SW	64	66	100	0	0	0	0	0	0
BP087	Ig1Eb	79	99	100	0	0	0	0	0	0
BP098	Ig1Eb	58	79	97	2	0	0	0	2	0
BP178	F1	284	83	100	0	0	0	0	0	0
BP109	F1	34	82	94	3	0	0	0	3	0
BR228	DomeYA	451	3	2	0	0	0	0	0	97
BR226	Dome OD	127	7	2	4	1	0	0	1	88

Eruptive units are from Hildreth & Wilson (2007).

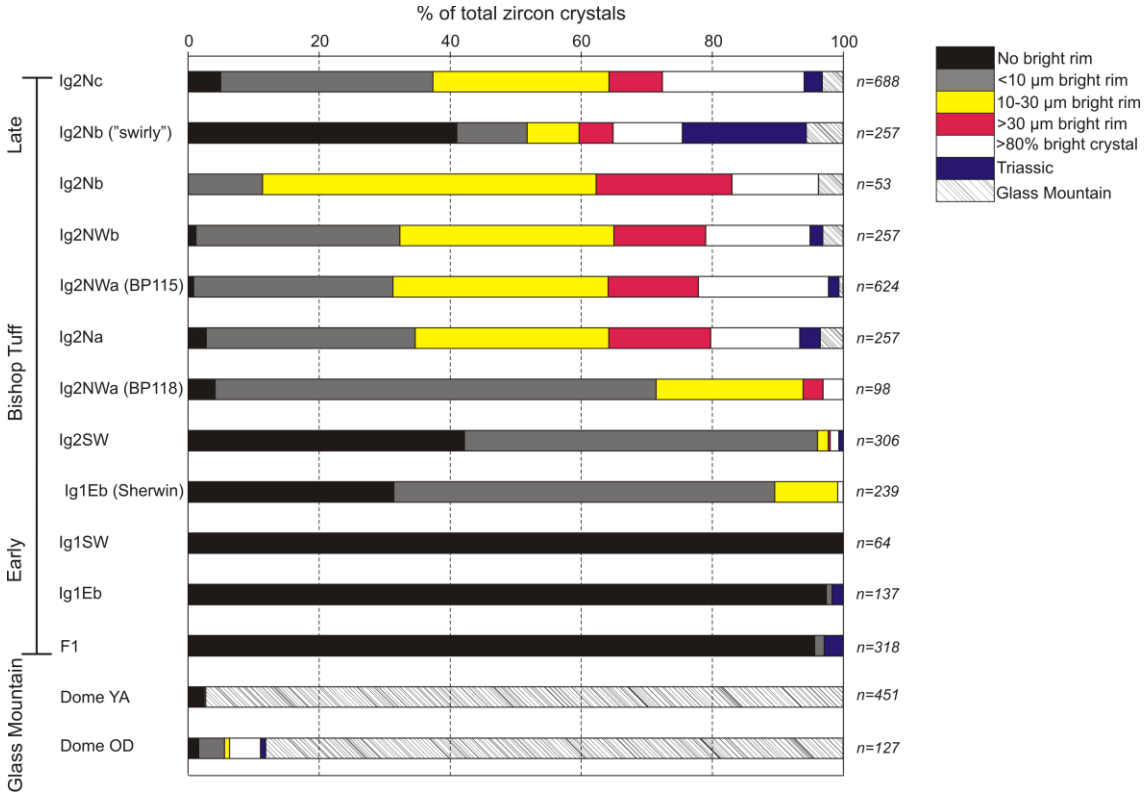

Fig. 3.4. Zircon CL zoning patterns (Fig. 3.3) correlated to stratigraphic position (from Wilson & Hildreth, 1997) within the deposits studied here. (Note the systematic changes through the Bishop eruption sequence from a dominance of 'normal Bishop'-type zircons with no bright rim to a dominance of zircons that have various degrees of development of the CL-bright rims.)

3.4.1.1. Sector Zoning

Sector zoning occurs both in non-rimmed grains and the cores of many bright-rimmed grains. Variable grey-scale intensities in the sector zoning dominate the CL images, whether oscillatory zoning is present or not (Fig. 3.3). Zircons from the fall units and early eastern ignimbrite lobes are dominantly (~85%) sector zoned, whereas the abundance of sector zoning diminishes to 24% in the latest unit (Ig2Nc). This diminution is gradual, with no sharp definable change corresponding to changes in eruption vent locations (Hildreth & Mahood, 1986; Wilson & Hildreth, 1997). Sector zoning is also common in zircons from the Ig1SW and Ig2SW units, previously been suggested to be from a source similar to (but not necessarily co-vented from) the early-erupted fall deposits and ignimbrite (Hildreth & Wilson, 2007).

3.4.1.2. Bright Overgrowths

Bright overgrowths on zircons become the dominant feature in northern-erupted units, where <5% of the crystals show no bright overgrowth, and ~65% of all crystals have >10 μm wide bright rims. The core-rim contact shows no evidence for dissolution of the crystal core (Fig. 3.3, Electronic Appendix 2), implying that ingress of the contrasting magma composition or any changes in physical conditions did not cause significant dissolution of pre-existing grains. The width of the bright rim generally increases in zircons from pumices later in the eruption sequence, with some crystals showing purely bright-CL characteristics (Fig. 3.4). Sector zoning is greatly subdued in the bright zones. The bright CL rims in zircons are inferred to be the counterparts to the bright rims reported from CL and BSE images on quartz and sanidine crystals, respectively (Peppard *et al.*, 2001; Morgan & Blake, 2006; Wark *et al.*, 2007; Pamukcu *et al.*, 2012). Bright rims on quartz and sanidine are generally reported only in the later units erupted from the northern caldera rim, although Gualda (2007) reported sparse bright-rimmed quartz and feldspar grains from the early-erupted sequences. Our observation that <10 μm bright rims are present in late Ig1Eb (Sherwin subunit of Hildreth & Wilson, 2007) and Ig2SW is in agreement with glass and melt inclusion chemistry (Roberge *et al.*, 2013) showing some degree of mixing in 'middle-erupted' units of the Bishop Tuff. Bright rims are not found in zircons from Glass Mountain dome YA, yet are sparsely present on crystals from dome OD. We infer that the magma from which the bright zones crystallised in zircon (and other minerals) is not simply a short-lived feature associated only with the Bishop Tuff magma body, but represents a recurrent feature.

3.4.1.3. Zircons from swirly pumices

Two pumices sampled were of the crystal poor, highly vesicular swirly type (Hildreth & Wilson, 2007), collected from Ig2Nb. Particularly high proportions (18 and 21%) of basement-derived zircons occur in these clasts; the grains wholly lack any overgrowths ('normal' or 'bright rim'), and are commonly fractured but always glass coated.

3.4.2 U–Pb age determinations

A total of 616 acceptable U–Pb ages were obtained on 12 samples of the Bishop Tuff, as well as 38 ages from Glass Mountain dome YA and 18 from dome OD. 'Acceptable' for the purpose of this study means analyses with <10% of the ^{206}Pb attributable to common Pb, regardless of the U concentration at the spot point. Single age determinations on grains

with U >500 ppm have 2σ uncertainties between 14 and 179 kyr, with an average of ± 48 kyr; however, when the analyses are combined in weighted mean estimates the uncertainties are greatly reduced.

3.4.2.1. Bishop Tuff: general age data

Age determinations, together with values for $^{206}Pb/^{238}U$ ratios, concentrations of U and Th, and the proportions of ^{206}Pb attributable to common Pb for all zircons analysed are given in Electronic Appendix 1. These data are annotated also for cores versus rims, sides versus tips of sector zoned grains, and binned for the bright rim widths. Zircons with a wide range of U concentrations were analysed (Fig. 3.5) although at lower U concentrations the analytical uncertainties increase and the proportions of ^{206}Pb attributable to common Pb often are beyond our 10% cut-off for acceptable analyses (see Methods section). Age determinations do not, within analytical uncertainties, increase at high uranium concentrations (Fig. 3.5) as has been reported elsewhere and attributed to the effects of metamictization or high trace element concentrations resulting in analyses of unknowns no

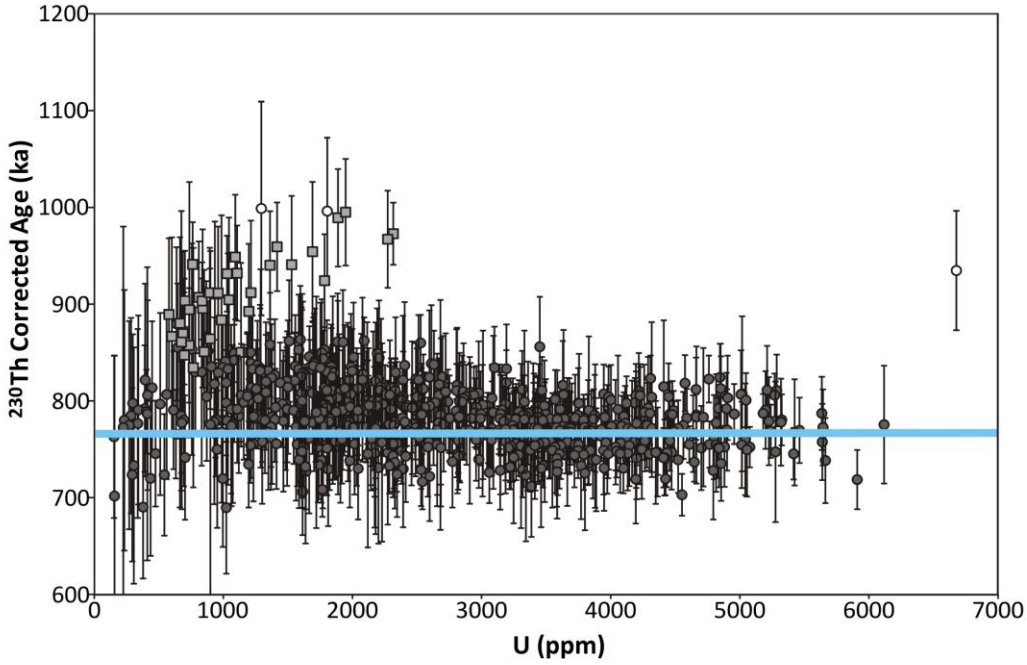

Fig. 3.5. U concentrations (ppm) versus ^{230}Th-corrected $^{206}Pb/^{208}U$ ages (ka) for all Bishop Tuff (circles) and Glass Mountain dome YA (squares) data points. The 3 open circles represent data points which fall outside of the bulk range of Bishop Tuff data and may be erroneous. The thick line indicates eruption age estimates from $^{40}Ar/^{39}Ar$ experiments on feldspar and ID-TIMS experiments on zircon (767 ka; see text for details and references). Error bars represent 2σ uncertainties.

longer being matrix-matched by the zircon standard (e.g. Gagnevin *et al.*, 2011; White & Ireland, 2012). Variations in U concentrations are not systematic with sample or eruptive timing (Electronic Appendix 1). Our age determinations for all Bishop eruptive units and all locations within crystals range from ~700 ka to ~880 ka. A probability density function (PDF) curve generated in Isoplot (Ludwig, 2008) for all acceptable Bishop age determinations shows a unimodal peak (Fig. 3.6), with an associated weighted mean value of 777.9 ± 2.2 ka (95% confidence limits), where 26 of 616 analyses were rejected (MSWD =2.1, probability = 0.00).

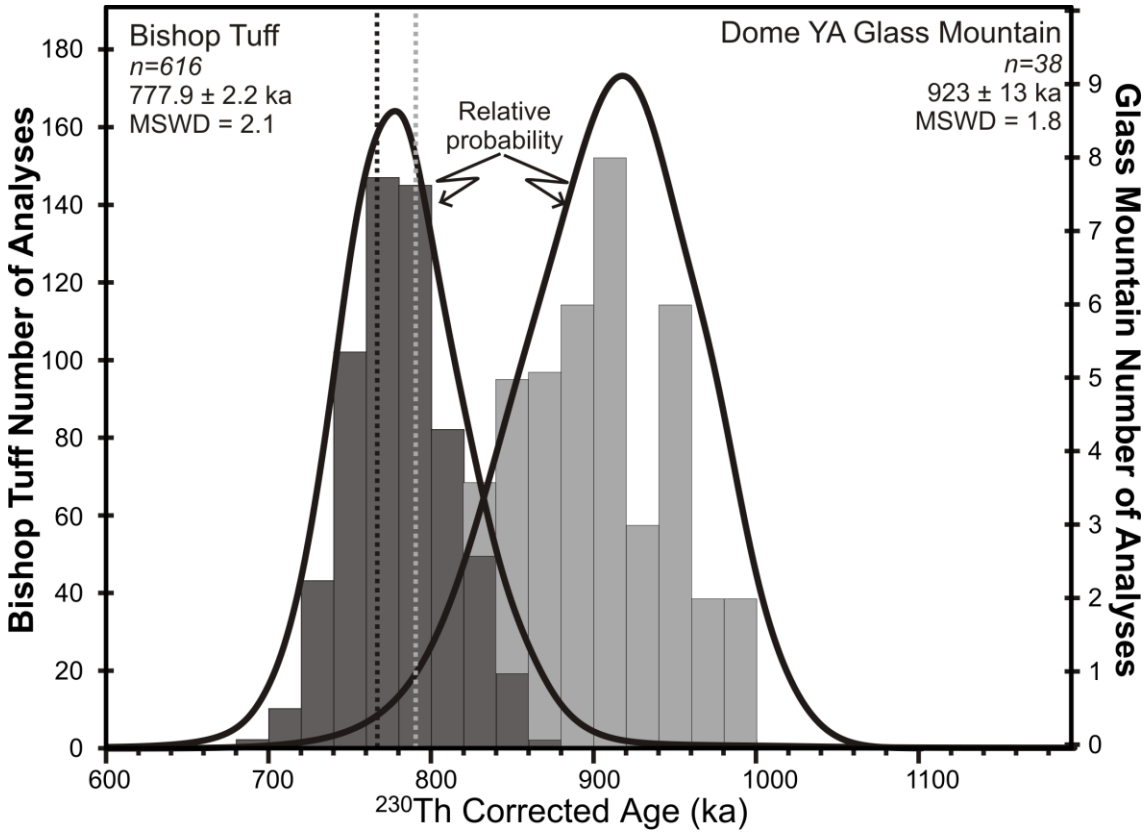

Fig. 3.6. Zircon ^{230}Th-corrected ^{206}Pb/^{208}U age data for the entire Bishop Tuff (dark grey), and for dome YA (Glass Mountain, light grey). The dashed lines are published eruption ages of the Bishop Tuff (767 ka; see text) and dome YA (790 ± 20 ka: Metz & Mahood, 1985). The probability density function (PDF) curve (from Isoplot: Ludwig, 2008) and histograms demonstrate the clear temporal separation between the youngest precursory Glass Mountain eruption and the Bishop Tuff. Values for the two data sets represent the number of spots used, and the weighted means, uncertainties at 95% confidence and mean squares of weighted deviates (MSWD) values for each population. For full data set see Electronic Appendix 1.

3.4.2.2. Bishop Tuff: details in age data

3.4.2.2.1. Sector-zoned ages. Given the dominance of sector zoning in zircons from early-erupted samples, we investigated whether the different sectors yielded the same ages for the same growth zones, as indicated by the 'growth rings' of oscillatory zoning. When sides and tips were compared there is no systematic age difference between sectors (Fig. 3.7): the CL darker tips yield a weighted mean of 773.5 ± 2.8 ka (nine of 267 rejected, MSWD=1.8) whereas the lighter sides have a weighted mean of 776.1 ± 7.2 ka (three of 60 rejected, MSWD=1.7). Side and tip ages within single crystals from samples BP098 and BP178, differ between the two sectors by <20 kyr for 13 of 22 crystals, but by 20 – 70 kyr for the others (Fig. 3.7; Electronic Appendix 1). When viewed together as part of a large sample suite it is apparent that there are no resolvable age differences between sides and tips.

3.4.2.2.2. Early- versus late-erupted units. Table 3.3 summarises weighted means for each of the 12 samples analysed for age. Four samples from F1 and lowest Ig1Eb representing 'early-erupted' material have age spectra with weighted-mean values ranging between 752.3 ± 5.7 ka and 776.1 ± 5.1 ka. In later-erupted samples the weighted means are somewhat older, ranging from 790.8 ± 8.5 ka to 825 ± 13 ka. When plotting single sample PDF curves through the eruption sequence, older ages are represented more in the later erupted material (see Electronic Appendix 1). However some bias has been introduced to analyses from zircons in the later-erupted samples owing to our specific targeting of cores within the bright-rimmed grains to ascertain whether they showed a longer crystallisation history (Simon & Reid, 2005). By separating core and rim analyses prior to calculating weighted means, we account for this bias.

3.4.2.2.3. Cores versus rims. In the four 'early-erupted' samples there is no significant difference in core versus rim ages, both yielding age-equivalent unimodal peaks (Fig. 3.8). Cores give a weighted mean of 774 ± 10 ka (one of 22 rejected, MSWD=1.6) and rims a weighted mean of 766.6 ± 3.1 ka (six of 172 rejected, MSWD=1.3). Three samples from the late-erupted Ig2Nb and Ig2Nc have rims that yield a slightly older weighted mean of 787.3 ± 5.2 ka (two of 62 rejected, MSWD=1.7). However, the cores of these late-erupted samples yield a bimodal PDF curve with a weighted mean of 807.5 ± 7.7 ka (three of 55 rejected, MSWD=1.4), which can be split into two age groups (<808 ka and >808 ka). The younger age group gives a weighted mean of 784.1 ± 8.7 ka (none of 27 rejected,

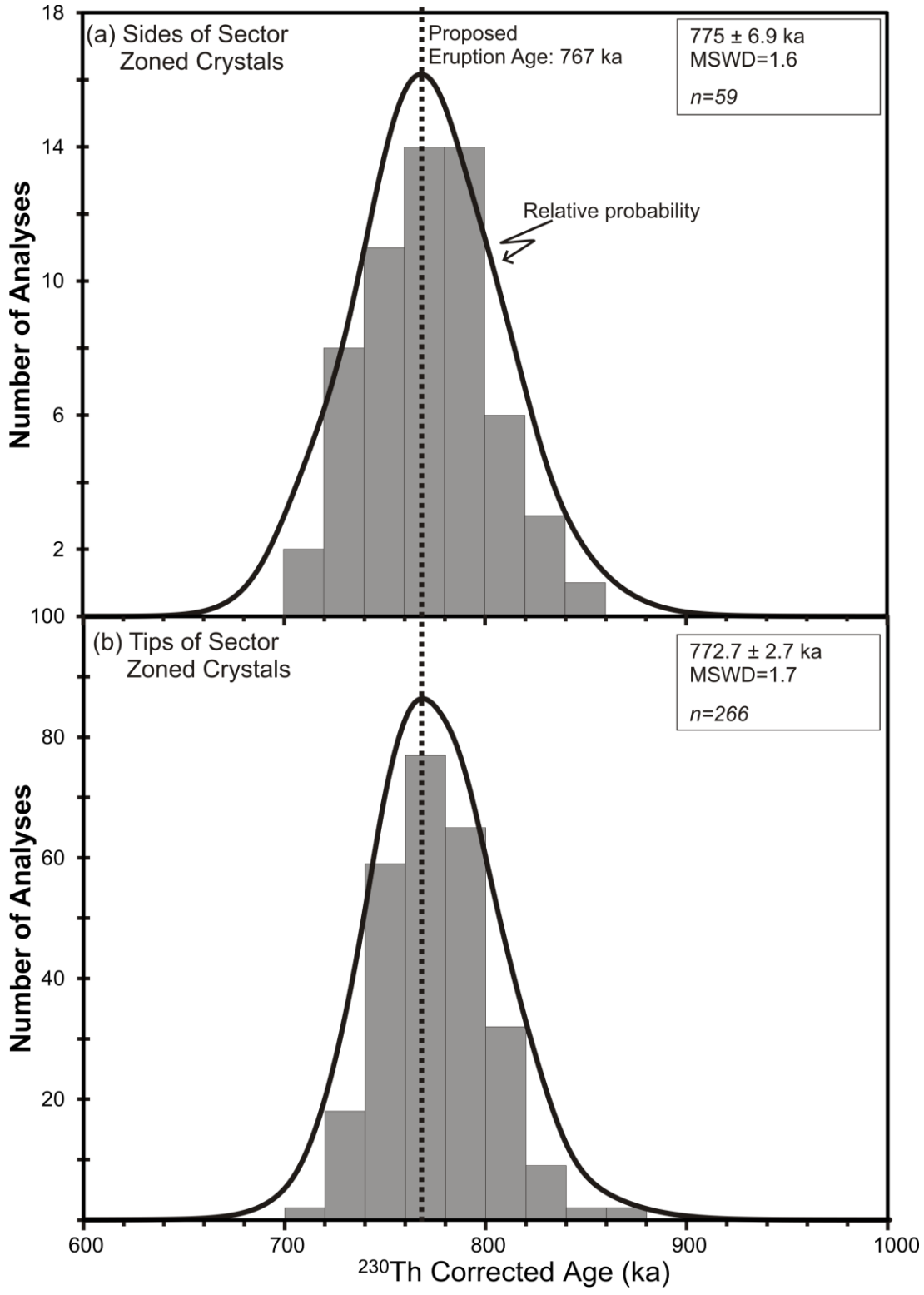

Fig. 3.7. Zircon ^{230}Th-corrected ^{206}Pb/^{208}U age data for all sector zoned zircons, to compare age determinations from the tips vs sides of the same crystals. Dashed line represents the proposed eruption age from ^{40}Ar/^{39}Ar experiments on feldspar and ID-TIMS experiments on zircon (767 ka; see text for details and references). Probability density function (PDF) curves from Isoplot. Values for the data sets represent the number of spots used (*n*), and the weighted means, uncertainties at 95% confidence and MSWD values for the respective populations. (For full data set see Electronic Appendix 1.)

Table 3.3. U–Pb ages measured using SIMS

Sample	Unit	Th/U ratio from LA-ICPMS analysis of glass		U (ppm)	Th (ppm)	$^{232}Th/^{238}U$	Total $^{206}Pb/^{238}U$	^{230}Th Corrected 206/238 Age (ka)	Error (2 σ) kyr
BP109	F1	2.5	average	3393	2134	0.6178	0.00011	770	46
			average "normal" core	3549	2487	0.6538	0.00011	781	45
			average "normal" rim	3301	1980	0.6027	0.00011	767	46
BP178	F1	2.5	average	3233	1986	0.5808	0.00011	773	40
			average "normal" core	3298	2181	0.6066	0.00011	790	42
			average "normal" rim	3357	1996	0.5752	0.00011	764	37
BP087	Ig1Eb	2.7	average	3685	2481	0.6697	0.00011	760	44
			average "normal" rim	3714	2517	0.6745	0.00011	760	43
BP098	Ig1Eb	2.7	average	3440	2039	0.5779	0.00011	777	42
			average "normal" rim	3416	2019	0.5759	0.00011	776	42
BP040	Ig1Eb-Sherwin	2.8	average	2845	1749	0.5918	0.00011	767	41
			average "normal" core	2429	1312	0.5191	0.00011	761	52
			average "normal" rim	3271	2145	0.6445	0.00011	758	41
BP059	Ig2Na	3.3	average	2404	1476	0.603	0.00011	796	50
			average "normal" rim	2913	1838	0.6151	0.00011	790	45
			average "normal" core	1654	877	0.5736	0.00012	816	60
			average "bright"	457	228	0.5278	0.00011	778	73
BP170	Ig2Nb	4	average	1414	733	0.536	0.00011	809	72
			average "normal" rim	1808	889	0.4971	0.00011	820	65
			average "normal" core	1534	738	0.4782	0.00011	814	69
			average "bright" rim	383	289	0.7005	0.00011	775	114
			average "bright" core	677	423	0.6486	0.00011	786	82
BP206	Ig2Nc	3.7	average	2073	1248	0.5739	0.00011	793	46
			average "normal" core	1864	1047	0.5665	0.00011	800	58

Table 3.3. Continued

Sample	Unit	Th/U ratio from LA-ICPMS analysis of glass		U (ppm)	Th (ppm)	$^{232}Th/^{238}U$	Total $^{206}Pb/^{238}U$	^{230}Th Corrected 206/238 Age (ka)	Error (2 σ) kyr
BP206	Ig2Nc	3.7	average "bright" core	942	436	0.4741	0.00011	809	49
			average rim	2979	1962	0.6315	0.00011	773	37
BP118	Ig2NWa	2.6	average	3003	2094	0.6746	0.00011	773	50
			average "normal" rim	3080	2149	0.6791	0.00011	771	49
			average "normal" core	3375	2727	0.771	0.00011	775	50
			average "bright"	2095	1300	0.6369	0.00011	783	71
BP115	Ig2NWa	3.1	average	1590	905	0.577	0.00011	802	54
			average "normal" rim	2600	1640	0.6383	0.00011	791	37
			average "normal" core	1548	783	0.5097	0.00011	817	42
			average "bright"	451	297	0.6526	0.00011	780	107
BP124	Ig2NWb	3.7	average	2410	1489	0.6225	0.00011	793	51
			average "normal" rim	3042	2031	0.6686	0.00011	794	45
			average "normal" core	2073	1190	0.5852	0.00011	794	57
			average "bright"	747	544	0.7627	0.0001	731	87
BP232	Ig2Nb (sw)	3	average	2930	2002	0.6785	0.00011	796	38
			average "normal" rim	3631	2484	0.6855	0.00011	790	31
			average "normal" core	2343	1550	0.6522	0.00012	816	41
			average "bright"	387	201	0.5384	0.00012	780	59
BR228	Dome YA	3.2	average	1099	512	0.4665	0.00013	928	71
BR226	Dome OD	2.3	average	8129	4569	0.5583	0.00026	1759	58

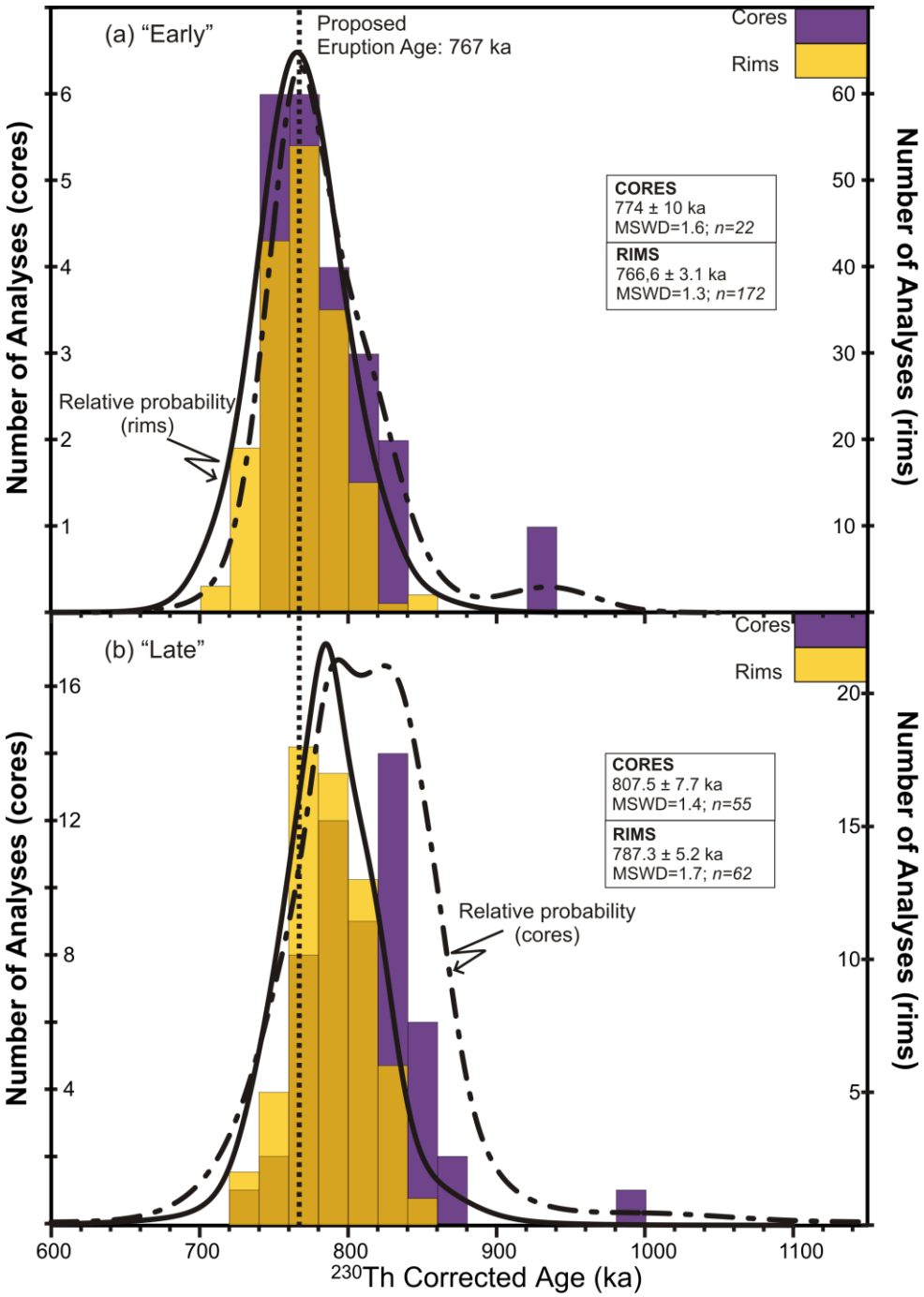

Fig. 3.8. Zircon ^{230}Th-corrected ^{206}Pb/^{208}U age data compared for spots in cores and rims from typical early and late-erupted samples. Dashed line represents the proposed eruption age from ^{40}Ar/^{39}Ar experiments on feldspar and ID-TIMS experiments on zircon (767 ka; see text for details and references). (a) Early erupted samples (F1-BP109 and BP178; Ig1Eb-BP087, see Table 3.1) have cores with a mean age that is closely similar to the rims from these samples. Both are within uncertainty of the independently determined eruption age estimates (see text). (b) Late-erupted rims from Ig2Nb/c (BP170, BP206 and BP232: see Table 3.1) samples are slightly older than eruption age, whereas cores show a marked tail-off to older ages. Probability density function (PDF) curve from Isoplot. Values for the data sets represent the number of spots used (*n*), and the weighted means, uncertainties at 95% confidence and MSWD values for the respective populations. For full data set see Electronic Appendix 1.

MSWD=0.42), whereas as the older age group yields a weighted mean of 838.5 ± 8.7 ka (none of 28 rejected, MSWD=0.75). When the 'unmix' option in Isoplot is applied to the data sets, two weighted means are obtained of 790.6 ± 10.0 ka and 836.9 ± 11.0 ka. Both of these approaches imply that there are two populations of grains, both distinctly older than those in the early-erupted samples, but which are indistinguishable on a textural basis.

3.4.2.2.4. Bright rimmed grains. Age determinations from the bright rims (Table 3.2) have greater uncertainties commensurate with the lower U and Th concentrations (sometimes <200 ppm: see Electronic Appendix 2). When plotted on a Tera–Wasserburg diagram, the collection of all low-U analyses with <30% of the ^{206}Pb attributable to common Pb yield a lower age intercept with a disequilibrium-corrected concordia value of 772 ± 28 ka (Fig. 3.9), matching the data from the higher-U grains or domains. Ages from the higher-U cores, but from spots sited just inside narrow (<10 μm) bright rims have a weighted mean of 777.5 ± 5.4 ka (five of 90 rejected, MSWD=2.3).

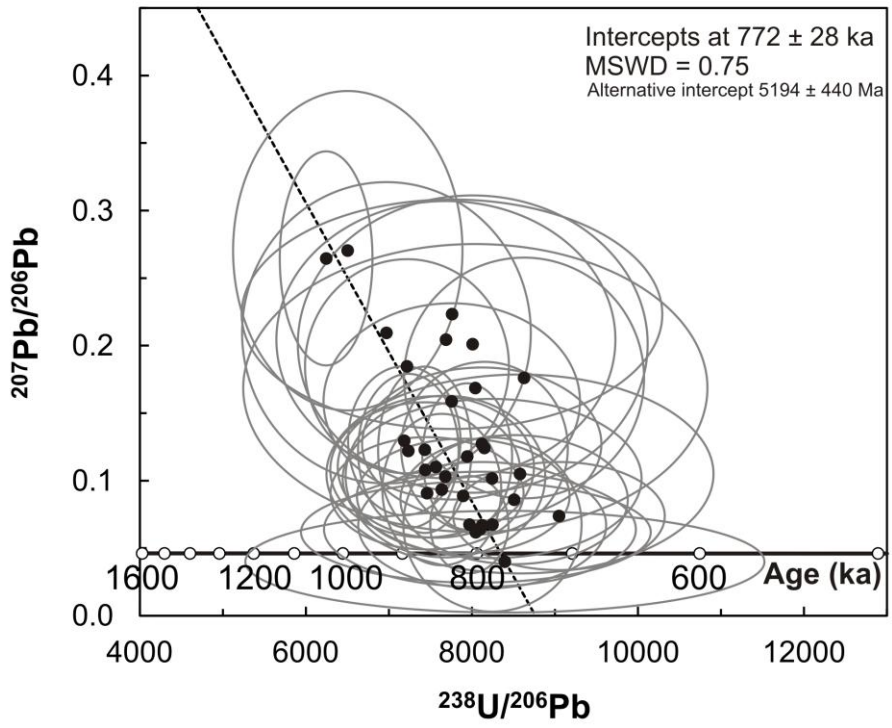

Fig. 3.9. Inverse isochron (Tera–Wasserburg) diagram generated in Isoplot of all analyses from grains with U<500 ppm and up to 30% of the ^{206}Pb attributable to common Pb, using the common-Pb composition for this age from the crustal evolution model of Stacey & Kramers (1975) (see text for discussion). The best-fit line is not pinned to any intercept value. Ellipses represent 2σ uncertainty on individual analyses. (For data set see Electronic Appendix 1.)

3.4.2.3. Glass Mountain samples

Eighteen ages for dome OD have a weighted mean of 1.750 ± 0.021 Ma (one of 18 rejected, MSWD=2.8: Table 3.3), similar to the 'minimum age' average of 1.728 ± 0.043 Ma (1σ, *n* = 4) from Simon & Reid (2005). Both figures are significantly older than the K–Ar eruption age of 1.35 ± 0.10 Ma (Metz & Mahood, 1985), but consistent with the $^{40}Ar/^{39}Ar$ age determination from step-heating experiments on sanidine of 1.702 ± 0.011 Ma (1σ) in Davies *et al.* (1994). [Note that Davies *et al.* (1994) report a value of 1.686 ± 0.011 Ma relative to a value of 1071 Ma for standard Hb3gr, for which Renne *et al.* (2011) give an age of 1081 ± 1.2 Ma.]. Zircons from dome YA yield 38 acceptable ages, one of which (1.682 ± 0.079 Ma) is inferred to be xenocrystic, despite having identical textural characteristics to the others. The 37 remaining ages range from 1000 ka to 820 ka and yield a unimodal PDF peak with a weighted mean of 923 ± 13 ka (none rejected; MSWD=1.8), somewhat younger than the average reported by Simon & Reid (2005) of 995 ± 19 ka (*n*=9, MSWD=2.2). A positive correlation of age versus U concentration is observed in the dome YA data (Fig. 3.5), in contrast to Bishop zircons, but we attribute this correlation to secular changes in the uptake of U into the grains, not to metamictisation or excessive trace element concentrations. The weighted mean for the youngest 30% of our age data yields a value of 862 ± 23 ka (*n*=12, MSWD = 0.096). We infer, based on previous work with New Zealand examples where eruption ages have been independently determined (e.g. Milicich *et al.*, 2013), that this value represents an accurate estimate for the eruption age of dome YA. This age is in contrast to the 790 ± 20 ka K–Ar determination by Metz & Mahood (1985).

3.4.3. Trace elements in Bishop zircons

Trace element analyses of zircons from seven Bishop Tuff samples were undertaken to characterise the trace element variation across the range of ages and CL characteristics, taking account of variations between sectors within single crystals as well as those between normal cores and the bright rims. Additionally, we collected trace-element data from the Mesozoic grains in sample BP232 (Ig2Nb: Table 3.1) to see if the compositional patterns differed significantly from those for the young grains. As in all microanalytical approaches to mineral chemistry, there is the risk of analyses reflecting contamination by melt or crystal inclusions. Although analytical spots were placed away from any visible inclusions, whether in CL images or in reflected light, in some cases it became apparent that inclusions

were intersected. We used common elements that are normally found at very low concentrations in zircon compared to the contaminant phase to monitor such contamination: Ca, Al, Na and K for feldspar and glass; Ca, P and F for apatite; Fe for Fe–Ti oxides; and Ca and Fe for allanite. Analyses showing significant degrees of contamination were culled accordingly. The full data are given in Electronic Appendix 3; spots with severe contamination are omitted, while others with minor contamination are highlighted and have suspect concentrations of affected elements struck through.

3.4.3.1. Bishop Tuff: general trace element data

When plotted all together, the trace element data form two contrasting end-member patterns (Fig. 3.10), between a single coherent array where intra-grain variations (see section below on sector zoning) fall within the overall trend of the array, or two separated but sub-parallel arrays. The overall trends in Fig. 3.10 reflect fractionation driven changes in the melt from which the zircons are growing (Reid *et al.*, 2011; Fig. 3.10a,b). It is typical for Ti and Th/U and Nd/Yb ratios to decrease and Yb/Gd to increase with increasing melt fractionation as measured by higher Hf concentrations or lower Eu/Eu* ratios. U typically covaries with Yb and the molar $(Y+Sc+REE^{3+})/P$ ratio (Belousova *et al.*, 2002; Claiborne *et al.*, 2006, 2010; Barth & Wooden, 2010; Barth *et al.*, 2012). Zircons from the earlier-erupted samples tend to have Eu/Eu* ratios around or lower than 0.01, whereas those from later-erupted samples have higher values due to crystallisation from a (still very-evolved) melt which has experienced slightly less feldspar fractionation (Reid *et al.*, 2011). The xenocrystic Triassic-age zircons follow the same general trends, but differ in values of Eu/Eu*, Yb/Gd and Th/U (Fig. 3.10e,f).

In contrast to the general fractionation-driven trends in Fig. 3.10, some elements or elemental ratios clearly plot as two parallel arrays. When subdivided into distinct groups the data reflect the overarching influence of sector zoning (Fig. 3.10). Two sub-parallel trends are apparent when Yb or another heavy REE (HREE), or the molar $(Y+Sc+REE^{3+})/ P$ (Fig. 3.10c,d), is plotted against U; these elements require careful consideration if magmatic trends are to be interpreted from these parameters.

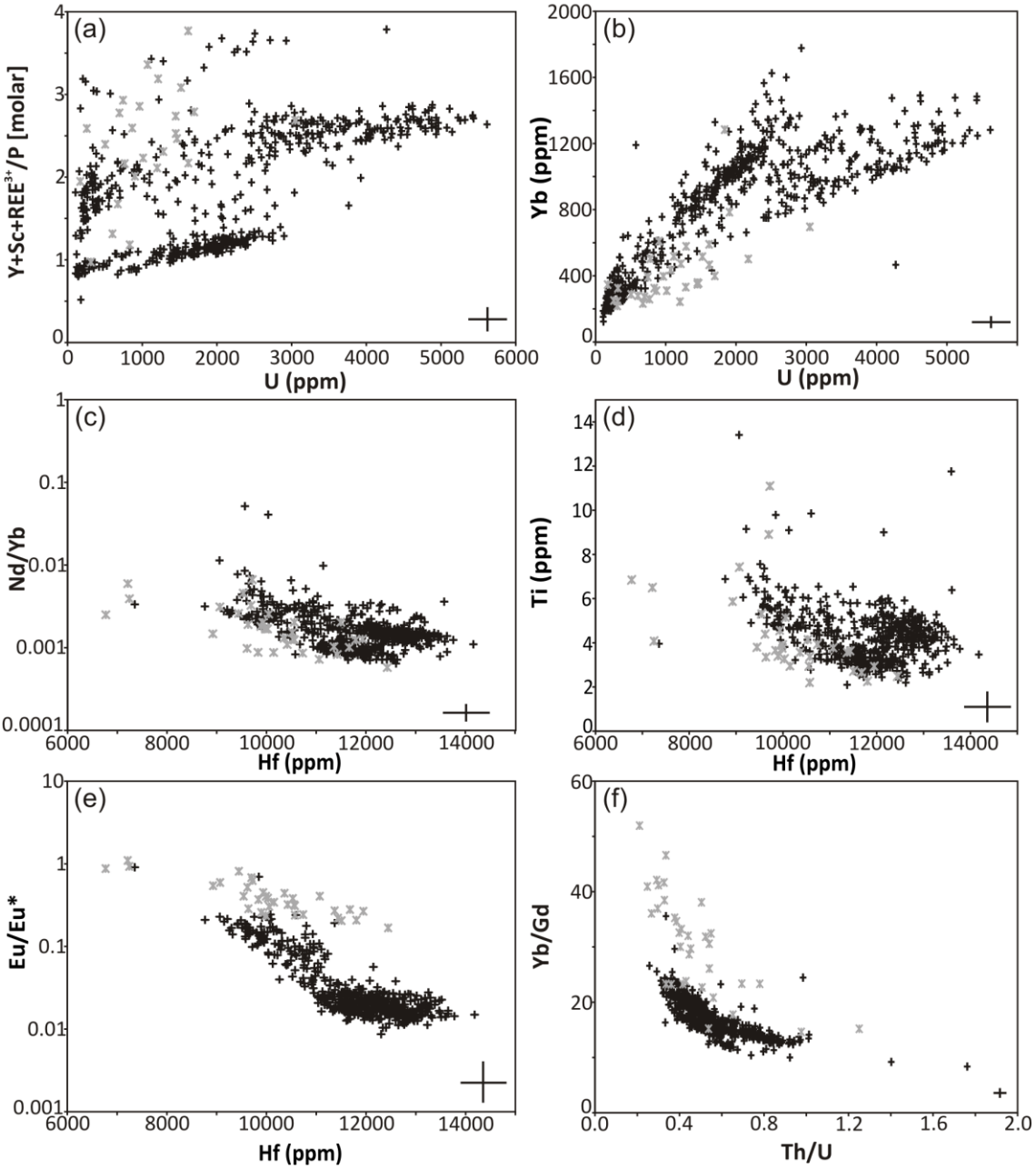

Fig. 3.10. Summary plots of zircon trace-element data from samples from the full range of the Bishop eruptive sequence. With certain trace elements or elemental ratios, sector zoning is clearly represented by the presence of split arrays (a, b), whereas its effect is subdued in other cases (c–f). Cross in bottom right of each panel represents 2σ uncertainties based on repeat analyses of the MAD green zircon (Barth & Wooden, 2010). Triassic-age grains are marked in grey, all Bishop data are in black. (For full data set see Electronic Appendix 3.)

3.4.3.2. Sector zoning contrasts

Whenever present, sector zoning strongly influences the distributions and abundances of many trace elements (Table 3.4; Figs. 3.10, 3.11). We have thus differentiated the data into those from crystal sides (growth along the *a*- and *b*-axes; lighter shades under CL) and from tips (growth along the *c*-axis; darker under CL) (Fig. 3.11). CL emission in zircons is primarily thought to be generated by Dy, Sm, Eu, Tb, Gd, Er and Nb, and can be suppressed by U, Y, Ca, P and Fe (Nasdala *et al.*, 2003). For the Bishop zircons that exhibit sector zoning, plots of many trace elements or their ratios against an element or ratio that can be used as an index of fractionation (e.g. Hf, Yb/Gd: Grimes *et al.*, 2009; Claiborne *et al.*, 2010; Carley *et al.*, 2011) define two arrays that might, in the absence of textural context, be interpreted as reflecting separate compositional suites. When compared with the lighter sides, the darker tips are enriched in Ti by ~45%, in the $(Sc+Y+REE^{3+})/P$ molar ratio by ~100% (Fig. 3.11a,b), in U and Th by up to about three times, and in Nb, U, Sm, Nd, Gd and Dy by 1.3 – 2 times (see Table 3.5 and Electronic Appendix 3). The lighter sides more closely follow the 'xenotime substitution' mechanism, where the molar ratio $(Y+Sc+REE^{3+}/P)$ is unity (Hoskin & Schaltegger, 2003; Reid *et al.*, 2011), whereas the darker tips show values of this ratio between 2.1 and 3.0, increasing with U, Th or Yb. This contrast between the different sectors appears to mostly reflect a relative depletion of P in the darker tips (Table 3.5, Fig. 3.11d).

Lighter sides have lower concentrations of trace elements in general, when compared with the dark tips. However, the separate data arrays for the two sectors are roughly sub-parallel in elongation and show similar evolutionary patterns. Some elements, such as HREE and Yb (Fig. 3.11e,f), are apparently less influenced by the sector zoning.

Table 3.4. Average and range in trace element concentrations for all samples analysed in the Bishop Tuff.

Sample	Unit	Location	P	Ti	Y	La	Ce	Nd	Sm	Eu	Gd
BP109	**F1**	**lighter sides**									
		average	1356	3.23	3224	0.013	44.6	1.27	5.08	0.096	58.7
		maximum	1529	3.71	4383	0.06	67	2.89	9	0.193	92
		minimum	1067	2.62	2120	0	25.7	0.67	3.23	0.041	33.6
		darker tips									
		average	743	4.73	3583	0.015	90.6	1.6	6.44	0.123	77
		maximum	944	5.92	4619	0.064	115.7	2.45	9.36	0.181	101.7
		minimum	630	4.05	2760	0.003	71.7	1.12	4.8	0.082	60.1
BP087	**Ig1Eb**	**lighter sides**									
		average	1309	3.1	3033	0.011	45.2	1.13	4.63	0.102	60.4
		maximum	1609	3.74	4924	0.021	94	4.17	12.92	0.281	156.1
		minimum	981	2.34	1864	0.003	23.7	0.54	2.47	0.054	30.3
		darker tips									
		average	714	4.63	3617	0.012	94.7	1.63	6.69	0.129	80.2
		maximum	838	5.4	4465	0.025	117.3	2	7.99	0.209	98.3
		minimum	471	3.69	2026	0.003	49.9	1.02	3.6	0.083	42.8
BP040	**Ig1Eb (Sherwin)**	**lighter sides**									
		average	1077	2.99	2964	0.012	40.1	0.95	4.07	0.089	51.7
		maximum	1688	3.6	3535	0.029	52.5	1.29	5.16	0.122	64.1
		minimum	448	2.44	2125	0.001	25.2	0.55	2.67	0.048	35
		darker tips									
		average	721	4.49	3577	0.012	90	1.55	6.63	0.115	79.1
		maximum	838	5.32	4522	0.03	114.2	1.96	8.39	0.148	98.3
		minimum	521	3.61	2257	0.002	52.2	0.83	4.09	0.084	49.8
BP059	**Ig2Na**	**lighter sides**									
		average	1227	3	2827	0.045	39.4	0.95	3.94	0.093	48.1
		maximum	1463	3.48	3676	0.137	52.1	1.6	6.37	0.13	65.7
		minimum	1021	2.49	1995	0.02	29.2	0.62	2.63	0.068	32.4
		darker tips									
		average	626	4.35	3147	0.038	85.4	1.52	5.71	0.13	67.2
		maximum	758	5.5	4104	0.09	121.8	2.14	7.79	0.17	92.5
		minimum	448	3.64	2152	0.016	57.6	1.17	3.47	0.074	42.6
BP170	**Ig2Nb**	**cores**									
		average	714	3.94	2377	0.026	58.1	1.46	4.72	0.135	50.2
		maximum	1245	6.09	4613	0.118	134.9	3.31	9.49	0.284	108.2
		minimum	359	2.71	1400	0.005	20	0.51	1.82	0.02	23.1
		bright rims									
		average	303	4.99	819	0.023	34.7	0.74	1.91	0.187	17.5
		maximum	684	6.8	1488	0.173	57.7	1.39	3.67	0.581	34
		minimum	146	3.13	327	0.004	20.3	0.27	0.79	0.05	7
BP118	**Ig2NWa**	**lighter sides**									
		average	1331	3.24	2936	0.014	42.1	0.95	3.96	0.092	49.4
		maximum	1688	3.73	4401	0.04	53.7	1.25	5.21	0.128	68.6
		minimum	1075	2.7	2126	0.003	33.9	0.67	3.03	0.073	39.6
		darker tips									
		average	686	4.75	3273	0.015	91.6	1.57	6.12	0.132	72.3
		maximum	872	5.37	4555	0.052	125.2	1.99	8.53	0.234	104.2
		minimum	489	4.1	1910	0.001	50.5	0.89	3.52	0.085	41
		cores									
		average	1043	4.16	2773	0.031	60.7	1.21	4.73	0.122	54.2
		maximum	1567	5.79	4049	0.153	108.1	1.8	8.07	0.172	91
		minimum	573	2.76	1871	0.004	28.9	0.57	2.51	0.076	33.1
		bright rims									
		average	459	5.2	1093	0.304	38.6	1.25	2.46	0.161	22.1
		maximum	1092	7.56	2230	1.896	53.8	3.17	3.95	0.324	40.7
		minimum	188	3.17	570	0.007	21.3	0.53	1.35	0.065	12.7
BP232	**Ig2Nb**	**cores**									
		average	1037	4.17	3369	0.037	70.2	1.52	5.47	0.149	66.6
		maximum	1583	5.59	4415	0.106	121.4	2.52	7.93	0.544	98.5
		minimum	368	2.9	1199	0.009	34.5	0.92	3.18	0.071	32.9
		bright rims									
		average	795	4.43	2559	0.055	48.2	1.51	4.63	0.197	51.1
		maximum	1618	7.84	4488	0.297	84.4	4.08	10.98	1.068	110
		minimum	110	2.67	636	0.013	23.7	0.62	1.64	0.063	14.8

Table 3.4. continued

Sample	Tb	Dy	Ho	Er	Tm	Yb	Lu	Hf	Pb	U	Th
BP109	**lighter sides**										
lt-av	127.1	23.7	297.7	591	129.2	1076	195.6	11817	0.189	2060	1010
lt-max	172	34.9	419.1	789.1	167.3	1393	245.9	12454	0.259	2671	1451
lt-min	83.3	14.8	191.2	410.9	92.9	801.2	146.2	11209	0.103	1415	534
	darker tips										
dk-av	144	29.7	353.8	646.7	138.3	1136	201.6	12577	0.363	3548	2232
dk-max	185.8	38.5	452.7	820.4	172.5	1397	249	13029	0.604	4547	3628
dk-min	111.8	23.7	281.5	501.8	107.4	867.9	152.6	11969	0.264	2733	1229
BP087	**lighter sides**										
lt-av	127.1	23.9	297.2	557.9	127.1	1054	191.9	11898	0.189	2013	983
lt-max	253.7	55.6	640.7	883.1	225.1	1777	308.9	12647	0.283	2927	1977
lt-min	73.3	12.5	159.5	341.4	77.3	654.7	124.1	11327	0.124	1197	384
	darker tips										
dk-av	145.7	30.5	360.2	644.4	135.7	1103	193.5	12692	0.388	4165	3190
dk-max	180.9	37.8	447.8	829.2	179.2	1491	262.6	13239	0.534	5434	4806
dk-min	82	16.3	195.6	373.7	79.5	662.5	119.7	12087	0.237	2144	957
BP040	**lighter sides**										
lt-av	20.8	266.6	116.7	541.1	119.6	1005	184.8	11945	0.183	1970	880
lt-max	24.9	320	139.2	639.2	139.9	1175	215.4	12552	0.274	2354	1130
lt-min	14.4	188.3	83.8	396.9	89.6	756.3	141.6	11591	0.122	1418	507
	darker tips										
dk-av	30.3	359.5	144.5	646.3	135.9	1112	196	12823	0.398	4170	3041
dk-max	37.6	449.6	186.5	836.1	178.5	1475	266.8	13094	0.492	5256	4534
dk-min	20	241.7	95.9	448.9	93.9	807.2	143.2	12580	0.308	2976	1982
BP059	**lighter sides**										
lt-av	111.6	20.7	266.2	544.8	120.9	1033	188	12241	0.188	1859	797
lt-max	145	28	359	720.2	157.9	1351	241.9	12805	0.304	2562	1214
lt-min	76.9	13.7	178.6	371.4	84.6	735.8	137.5	11719	0.089	1141	422
	darker tips										
dk-av	127.5	26.9	327.9	595	127.5	1060	185.6	13150	0.374	3463	2370
dk-max	168.4	36.8	444.4	778.2	167.5	1393	241.1	13774	0.538	4883	4235
dk-min	86.9	17.3	218	420.8	93.2	783.1	143.7	12563	0.15	1448	582
BP170	**cores**										
c-av	94.4	19.1	228.4	432.2	93.3	773	140.4	11739	0.16	1536	972
c-max	180.9	41.2	475.9	822.1	173.1	1385	238.8	12302	0.53	5148	4988
c-min	52.3	9.3	119.6	251.5	57.1	487.1	90.1	10428	0.041	655	249
	bright rims										
br-av	32.7	6.5	77.4	156.1	35.2	304.9	58.8	10309	0.053	362	184
br-max	65.4	13.8	165.5	320.6	70.7	598.1	110	12228	0.182	1185	638
br-min	12.6	2.3	30	61.5	13.7	123.6	25.1	9296	0.008	110	49
BP118	**lighter sides**										
lt-av	110.1	20.1	254.6	517.6	114.3	956.3	175.5	11588	0.182	1757	859
lt-max	155	28.4	357.8	723.3	160	1312	236	12284	0.288	2747	1400
lt-min	82.6	15.3	189.8	379.9	82.9	712.7	133.3	10771	0.109	1234	585
	darker tips										
dk-av	132.4	27.7	329.8	594.4	125.9	1027	181	12429	0.351	3500	2612
dk-max	185	40.1	471.2	842	176.7	1463	252.5	12908	0.503	5423	4479
dk-min	77.4	15.8	188.1	352.9	76.2	636.9	115.8	11438	0.213	1918	1060
	cores										
c-av	108.9	21.3	259.7	501.6	109.1	912.1	166	11621	0.19	2029	1235
c-max	164	34.7	405.8	735.6	155.4	1289	225.9	12239	0.306	3789	2697
c-min	71.2	13.4	165.7	326.6	72.5	606	114.5	10939	0.101	838	386
	bright rims										
br-av	43	8.4	101.3	202.9	45.2	385.7	72.5	10608	0.069	522	262
br-max	86.4	15.9	197.4	400.4	88.4	756.5	139.2	11179	0.105	945	489
br-min	22.2	4.6	52.5	105.3	24.1	210.7	39.6	9514	0.037	196	111
BP232	**cores**										
c-av	131.2	25.9	316.7	601.8	128.3	1077	190.2	11876	0.314	2716	1739
c-max	171.7	37.5	438.1	770.9	165	1350	237.1	13035	0.653	5320	5015
c-min	47.6	10.6	120.3	225.2	48.3	422.5	78.4	9651	0.045	265	172
	bright rims										
br-av	100.9	19.8	242	471	101.6	863.5	154.9	11309	0.203	1751	915
br-max	182.1	40.5	467.4	836.6	172.7	1407	241.2	13605	0.49	4113	2900
br-min	25	5.1	62.4	119.8	26.7	241.4	45	7354	0.018	156	100

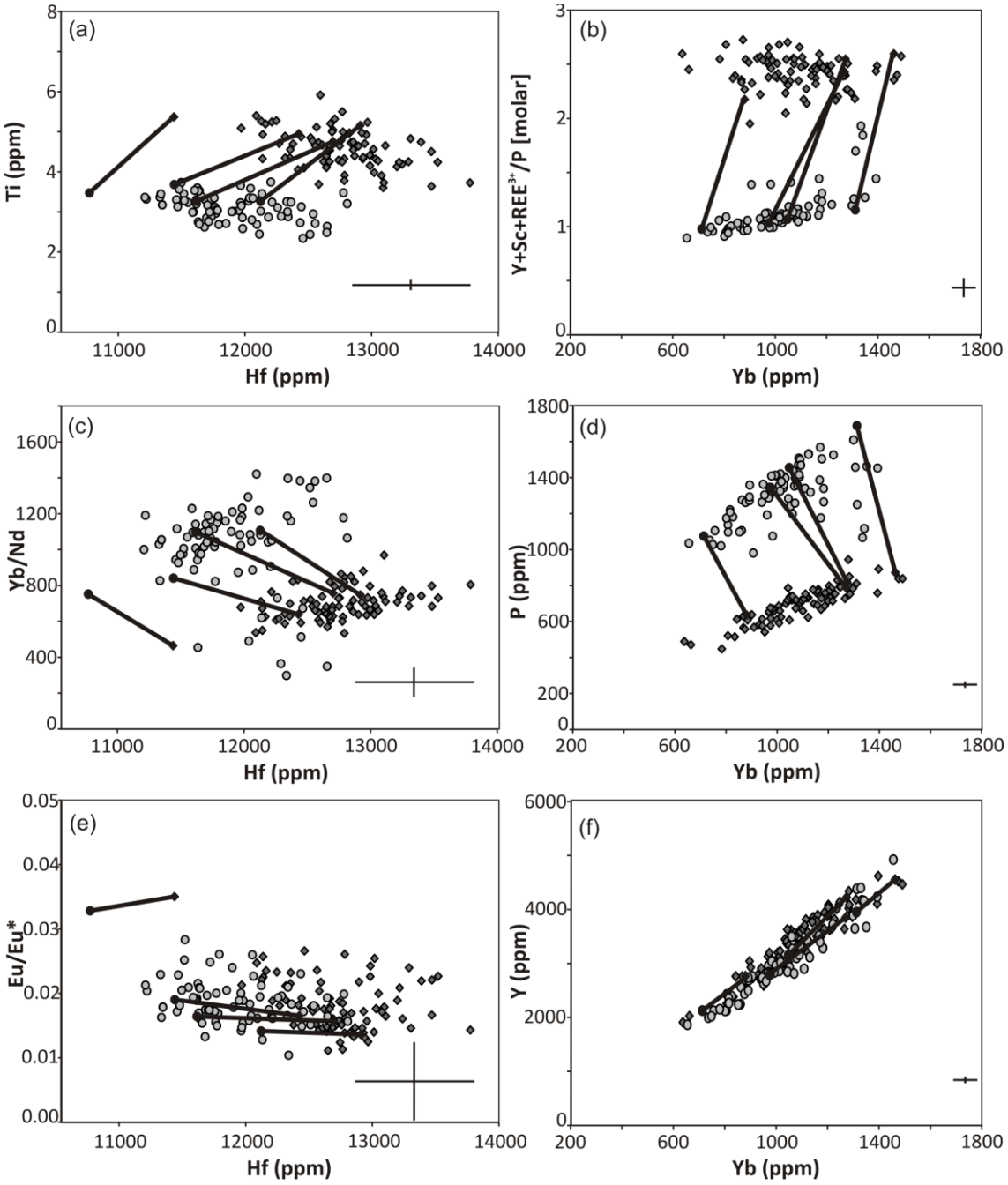

Fig. 3.11. Compositional variations within zircon crystals with textures dominated by sector zoning: dark grey diamonds represent darker tips; light grey circles represent lighter sides. Representative tie-lines connect sides and tips of single crystals. Cross in bottom right of each panel represents 2σ uncertainties. (For full data set see Electronic Appendix 3.)

Table 3.5. Enrichment factors for the dark tips in sector-zoned zircon crystals when compared to the lighter sides, arranged in order from most enriched to least enriched. An enrichment factor of 1.00 shows no enrichment. Factor <1 indicates depletion in the dark tips; a factor > 1 shows enrichment.

Element	Dark Tip Enrichment Factor
Th	2.61
Nb	2
U	1.75
Nd	1.56
Sm	1.42
Ti	1.37
Gd	1.37
Eu	1.32
Dy	1.22
Tb	1.21
Ho	1.35
Y	1
Yb	1
Tm	1
Sc	1
Lu	1
Hf	1
Er	1
P	0.75
$Y+Sc+REE^{3+}$:P	1.88

3.4.3.3. Core–bright-rim contrasts

In zircons that lack a bright rim, sector zoning dominates the variations in trace-element patterns. However, where bright rims were wide enough to analyse [three samples: from Ig1Eb (BP040), Ig2NWa (BP118) and Ig2Nb (BP170)] it is clear that the normal, sector-zoned Bishop cores (as defined on textural grounds) are enriched (on average) by ~50% in middle REE (MREE), Th and U relative to the bright rims (Fig. 3.12a,b). Although the absolute enrichment differs when bright rims are compared to dark tips or light sides, the enrichment is nonetheless present, and therefore we use an average of the sides and tips to calculate our enrichment factors. The bright rims crystallised from less evolved melts, displaying higher Eu/Eu* ratios (0.05 – 0.2) than the normal sector-zoned cores (0.01–0.04; Fig. 3.12c), indicative of a melt that had experienced less feldspar fractionation than the cores they overgrew. However, although the absolute concentrations show variability, several elemental ratios show no variation between cores and bright rims, for example, Yb/Gd vs Th/U (Fig. 3.12d). The bright rim analyses do not display as significant an influence of sector zoning on trace-element distributions; only a single trend in trace element patterns is defined, unlike the sub parallel trends seen in 'normal' Bishop grains (see previous section and Fig. 3.11).

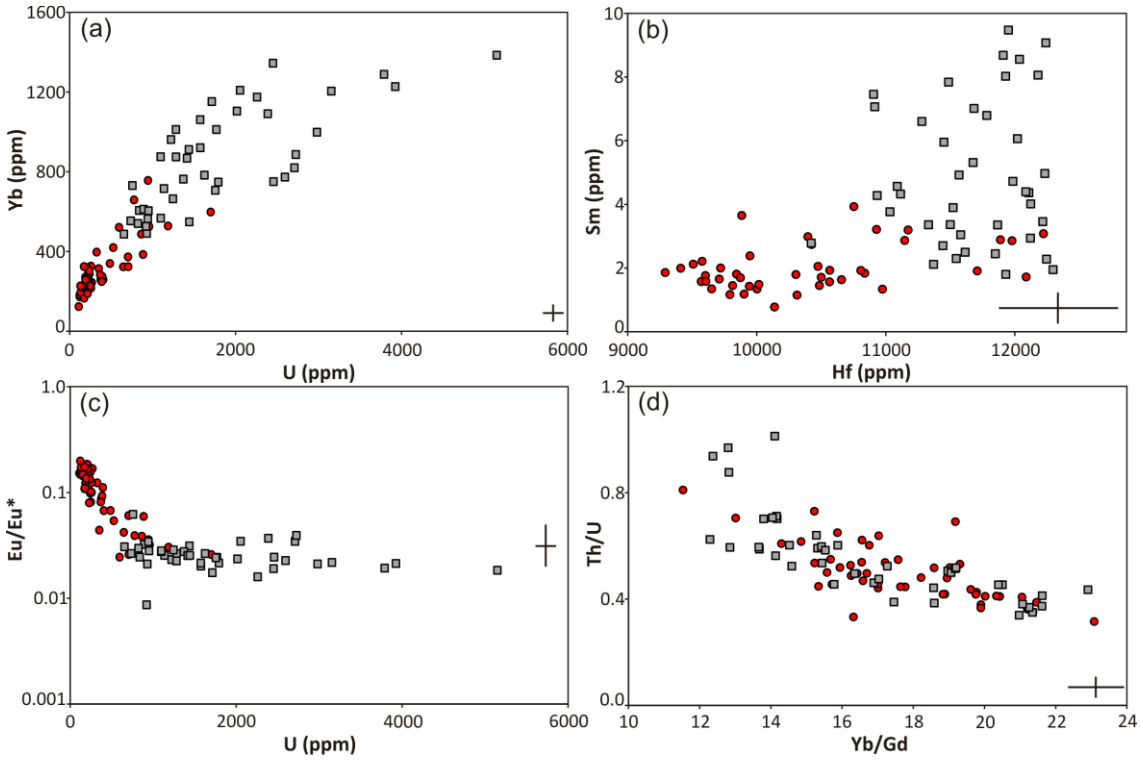

Fig. 3.12. Representative trace element compositional variations in CL-darker cores vs CL-brighter rims within Bishop zircon crystals. Cores are grey squares, rims are filled red circles. Cross in bottom right of each panel represents 2σ uncertainties. (For full data set see Electronic Appendix 3.)

3.5. Discussion

As emphasised by Hildreth (1977, 1979), zircon was among the first crystallising mineral phases in the Bishop magma. Integration of the information available from single zircons is thus relevant to the origins and evolution of the Bishop system across the entirety of its lifespan as a felsic, zircon-saturated entity.

3.5.1. Zircon chronological information in the Bishop Tuff

3.5.1.1. Eruption age of the Bishop Tuff

Recent studies on the Bishop Tuff have raised issues regarding the eruption age, primarily from comparisons between $^{40}Ar/^{39}Ar$ age determinations on feldspar and ID-TIMS determinations on zircon (e.g. Sarna-Wojcicki *et al.*, 2000; Crowley *et al.*, 2007; Rivera *et al.*, 2011; Singer *et al.*, 2012). This apparent conflict arises from two independent aspects:

(1) controversy over the appropriate values for the ^{40}K decay constant and consequent ages for the Fish Canyon (FCT) sanidine standard that is a benchmark for most young $^{40}Ar/^{39}Ar$ age experiments (e.g. Kuiper *et al.*, 2008; Renne *et al.*, 2010, 2011; Rivera *et al.* 2011);

(2) debate over the comparisons between single-crystal ID-TIMS age determinations and those obtained by spot analyses using SIMS techniques (Simon & Reid, 2005; Crowley *et al.*, 2007). This second debate in turn focuses on three issues: (1) the contrasting precisions obtainable by each technique, (2) the possibility of inheritance of grains with significant residence histories, skewing age determinations and populations towards older values, and (3) the three orders of magnitude contrasts in sample volume between the half- or whole-crystals analysed by ID-TIMS [(~1-3) x 10^6 μm^3] versus the small volumes [(~1.5-2) x 10^3 μm^3] excavated by SIMS analysis (see Crowley *et al.*, 2007; Simon *et al.*, 2008; Reid *et al.*, 2011; Reid & Schmitt, 2012).

We obtain a weighted mean age of 766.6 ± 3.1 ka (95% confidence) for grains that we have analysed in cross-section as close to the rims as feasible. These grains, which lack CL-bright overgrowths, come from samples in early-erupted material and hence represent the closest approximation we can make to measuring immediately pre-eruptive ages. Our mean value is the same, within uncertainty, as the weighted mean of 767.1 ± 0.9 ka (2σ) from ID-TIMS work on single grains (Crowley *et al.*, 2007), and the published $^{40}Ar/^{39}Ar$ age of 767.4 ± 2.2 ka (2σ) of Rivera *et al.* (2011), the latter based on a value for the FCT standard of 28.172 ± 0.028 Ma modified from Kuiper *et al.* (2008). Our data are, in turn, not in agreement with the older ages suggested for the Bishop eruption by Renne *et al.* [(2010, 2011: 778.1 ± 7.4 ka (2σ), based on re-calculation of the original data of Sarna-Wojcicki *et al.*, 2000)] and Mark *et al.* (2012: 776.4 ± 1.8 ka, 2σ). These differences are not bridged in our $^{206}Pb/^{238}U$ age determinations by the Th/U melt values adopted (Table 3.1) and its influence on the initial ^{230}Th disequilibrium correction. Comparisons between the range of melt Th/U ratios we use versus the uniform 2.81 value used by Crowley *et al.* (2007) indicate that ^{230}Th-corrected age values are 2 – 3 ka younger for Th/U = 2.5 (typical of early eruptives) and 6 – 8 ka older for Th/U = 4.0 (the maximum for later eruptive rocks: see Electronic Appendix 1).

Hence, despite the markedly different sampling strategies employed by SIMS and ID-TIMS, the results are identical within uncertainties. However, we note that there are some discrepancies in the data sets that could have produced systematic bias. The SIMS data clearly resolve the appropriate common Pb composition because there is no blank Pb to consider. As such, we clearly establish that the common Pb in the zircons (at the attogram-

femtogram level) is magmatic and not surface related. The common Pb value that we obtain from the inverse concordia plot of our common-Pb-rich data points is consistent with value from Stacey & Kramers (1975) used in SQUID 2, and also within uncertainty the same as the published bulk rock value of $^{207}Pb/^{206}Pb = 0.818$ derived by Halliday *et al.* (1989) and used by Simon & Reid (2005). Conversely, the ID-TIMS data relies on the common Pb being from the laboratory blank at the appropriate composition (see Crowley *et al.*, 2007, their supplementary data Table 1). In addition, our SIMS data utilizes Th/U compositions of the glass phase from the respective samples to make sample-specific Th/U fractionation corrections to the raw ^{238}U-^{206}Pb ages (see Table 3.3 and Electronic Appendix 1, which show the differences in age determinations between sample specific Th/U ratios and a constant Th/U ratio of 2.81). On the other hand, the ID-TIMS data use an averaged Th/U value from the data of Anderson *et al.* (2000) with which to calculate the age correction for initial ^{230}Th disequilibrium. The coincidence of the final ages from the two techniques indicates that common Pb and Th/U fractionation is treated appropriately in both data sets.

Although the precisions we obtain are an order of magnitude poorer than those from single-crystal ID-TIMS work, the utility of SIMS instruments to undertake orders of magnitude more analyses in the same time span and to give spatially resolved ages within single crystals, offers a complementary perspective that is, in this case, in agreement. As highlighted by Reid & Schmitt (2012), bulk ID-TIMS analysis is a whole-grain average, weighted by the U (and Pb) contents of the individual zones which compose the crystal. Volumetrically small core zones could therefore be completely dominated by the large outer growth zones (Charlier & Zellmer, 2000). Another aspect that arises is comparisons between surface profiling techniques (e.g. Reid *et al.*, 2011; Storm *et al.*, 2011; Reid & Schmitt, 2012) and the cross-sectional techniques we have employed, with the outermost rims being argued to yield a 'true' U–Pb eruption age owing to there being no influence from older cores. Reid & Schmitt (2012) reported an average of SIMS surface profiling ages from Bishop zircons of 781 ± 22 ka (uncertainty inferred by us to be 2σ). With cross-sectional analysis we can thus replicate as good an approximation to eruption age as the uncertainties on the measurements allow, despite not analysing the outermost parts of any crystal. With both approaches (e.g. Charlier *et al.*, 2005; Storm *et al.*, 2011), however, there are commonly grains within samples that have inherited ages, whether through their recent (re-)introduction into the magma as antecrysts from the underlying mush pile or xenocrysts

from country rock. In either case, the scatter of ages obtained may reflect subtle issues of inheritance, not just position within the crystal or the uncertainties associated with single age determinations.

3.5.1.2. Temporal relationships between Glass Mountain and the Bishop Tuff

A previous tenet of the magmatic history at Long Valley is the temporal continuity and close compositional relationships between the younger series of eruptions from Glass Mountain and the Bishop Tuff. The YA dome K–Ar age of 790 ± 20 ka (Metz & Mahood, 1985) has been accepted by all workers and has been used to consider that there was temporal overlap of the Bishop and Glass Mountain systems. Our data suggest, in contrast, that the two systems are separate in time and distinct, with our estimate of 862 ± 23 ka for the eruption age of dome YA.

Other data also support an older age for the cessation of Glass Mountain activity (Sarna-Wojcicki *et al.*, 2005). An averaged single-crystal sanidine $^{40}Ar/^{39}Ar$ age of 890 ± 31 ka [adjusted relative to a Taylor Creek sanidine standard age of 28.485 ± 0.033 Ma to match Rivera *et al.* (2011)] was reported by Sarna-Wojcicki *et al.* for their bed BT-16, underlying the Bishop Tuff at Chalk Bluffs. This sample was reported by them as yielding the youngest reliable (i.e. uncontaminated) age for pre-Bishop fall deposits at this location. The older eruption ages suggested by our zircon ages for domes YA and OD [the latter matched by the $^{40}Ar/^{39}Ar$ age determination in Davies *et al.* (1994)] imply that the entire Glass Mountain system may be significantly older than previously reported. A revision to the age spread for the Glass Mountain complex therefore could suggest the older $^{40}Ar/^{39}Ar$ dated tephras of Sarna-Wojcicki *et al.* (2005) in the Blind Spring Hill area were early products of the Glass Mountain system, rather than from an as-yet unknown older system in Long Valley.

In comparison, a weighted mean estimate for the oldest 10% of our acceptable Bishop zircon ages (all of which are core analyses) is 844 ± 6 ka (n = 62, MSWD = 0.78, probability of 0.89: data points shown in Fig. 3.5). This age is indistinguishable from the older population of cores from the northern units derived by unmixing (838.5 ± 8.7, Fig. 3.7). We thus infer on the basis of age data, coupled with qualitative observations of the zircon textures, that the Glass Mountain and Bishop systems were not only temporally but also physically separate entities. Such a view is not in conflict with abundant evidence for

their chemical continuity, on the basis of compositional and isotopic data for the younger Glass Mountain activity, from ~1.1 Ma onwards from published K–Ar ages (e.g. Halliday *et al.*, 1984, 1989; Metz & Mahood, 1991; Bindeman & Valley, 2002; Simon *et al.*, 2007). We would contend, however, that growth of the Bishop zircon population and assembly of the Bishop melt-dominant body post-dated and were separate from the youngest activity from the Glass Mountain system.

3.5.1.3. Assembly of the Bishop magma body

We interpret our age data to show that crystallisation of Bishop magma began from 844 ± 6 ka (as above) and continued up to the time of eruption, at 766.6 ± 3.1 ka. Previous workers have reported age ranges consistent with a prolonged crystallisation history of zircons in the Bishop Tuff of ~160 kyr (Reid & Coath, 2000; Simon & Reid, 2005). Peak PDF estimates (2σ uncertainties) of 823 ± 28 ka (early Bishop Tuff), and 811 ± 14 ka (late Bishop Tuff) can be calculated from the data of Reid & Coath (2000) and 841 ± 16 ka (early Bishop Tuff) from Simon & Reid (2005). It has been inferred that both the early- and late-erupted Bishop units had a history of zircon crystallisation extending as far back as 900 ka, with average maxima of 917 ± 27 ka for the early Bishop Tuff and 901 ± 17 ka for the late Bishop Tuff (Simon & Reid, 2005), and a value of 892 ± 26 ka reported by Reid & Schmitt (2012). In contrast, we can see evidence for only ~80 kyr of crystallization history in the overwhelming majority of zircons within the tuff.

The older suite of ages we obtain (Fig. 3.8 and Electronic Appendix 1) from zircon cores, particularly from pumices erupted later and from the northern vents, are inferred to represent the onset of zircon crystallisation within the Bishop mush zone: that is, the onset of crystallisation for most of the mineral species represented in Bishop pumices (Hildreth, 1979). What cannot be discerned from our data alone is whether this onset of zircon growth accompanied or pre-dated growth of the melt-dominant, stratified body. Overall growth rates for Bishop zircons implied by our age data are similar to the generalised 10^{-18} – 10^{-19} m s^{-1} value for granitic melts by Watson & Liang (1995), and grains from the 844 ka average-age suite show no differences in texture from those yielding ages within uncertainty of the eruption age. Where possible, zircons with a narrow (<10 μm) bright rim were dated at spots within the 'normal' sector-zoned Bishop interior, directly adjacent to the bright rim. These ages give the oldest age for the bright rim (in those thinly rimmed crystals), and thus the difference in the weighted mean of these ages (777.5 ka) from the

proposed eruption age (766.6 ka) can be used as the maximum time for growth of a 10 μm (or less) rim. This age difference yields a maximum growth rate of ~3 x 10^{-19} ms^{-1} (up to 1.3 x 10^{-18} ms^{-1}, and as slow as 1.6 x 10^{-19} ms^{-1}, with uncertainties), assuming no dissolution or cessation of zircon growth occurred during that time. If the zircons across the age range from 845 to 766 ka grew in contrasting physical environments (i.e. a crystal-dominated mush versus a melt-dominant magma body) then these contrasts have left no distinctive textural or compositional signals.

3.5.2 .Zircon compositional information in the Bishop Tuff

3.5.2.1. Implications of sector zoning variations

The ubiquitous sector zoning observed in zircons from early-erupted samples and in the cores of many crystals in samples from the northern ignimbrite lobes is in contrast to the more homogeneous CL textures generally documented in dated zircons (e.g. Corfu *et al.*, 2003; Munoz *et al.*, 2012). Experimental studies that investigated sector zoning and trace-element uptake in pyroxene, titanite and zircon have found that these minerals have apparent partition coefficients that vary depending on the crystal face (Paterson & Stephens, 1992; Watson & Liang, 1995; Lofgren *et al.*, 2006; Schwandt & McKay, 2006). It has been proposed that if the crystal growth rate is fast enough to 'trap' trace elements at the crystal-melt interface, and diffusivity of elements within the crystal lattice is not rapid enough to eradicate differences in concentration, sector zoning is generated (Watson & Liang, 1995; Watson, 1996). However, such conditions are almost always met in volcanic zircons regardless of whether or not sector zoning is visible in CL imagery. Sector zoning is not as obvious in the Glass Mountain or the bright-CL Bishop zircons, suggesting that there were differences in the crystal growth regimes when compared with the normal Bishop sector zoned grains.

The differences in trace elements between different sectors in the normal Bishop zircons raise questions about the relevant substitution mechanisms. Although the lighter sides have molar $(Y+Sc+REE^{3+})/P$ values of ~1 [the 'xenotime substitution' of Hoskin & Schaltegger (2003)], the darker tips have considerably higher values (Figs. 3.11a; 3.13a), in large part due to a depletion in P. Although it is beyond the scope of this paper to suggest an alternative substitution mechanism, it appears that the xenotime substitution may only be operable on certain crystal faces along the *a* and *b*-axes (100 and 010 in the tetragonal grains we are dealing with here) (Hoskin & Schaltegger, 2003). It is therefore possible that

P fits better, and Y and the larger REE somewhat less well, into the lattice configuration along the 100 and 010 faces than the faces intersecting with the *c*-axis. An alternative charge-balancing scheme for crystallization in the dark sectors may need to be considered.

3.5.2.2. Ti concentrations and Ti-in-zircon thermometry

Our data show that the Ti concentrations in the same growth zone (as indicated by oscillatory zonation patterns) in sector zoned zircons varies significantly between the sides and tips. This has strong implications for the applicability of Ti-in-zircon thermometry to the Bishop Tuff. As currently formulated, a single value of the activity of TiO_2 in the magma ($aTiO_2$) is adopted when applying the Ti-in-zircon thermometer (Watson & Harrison, 2005; Watson *et al.*, 2006; Ferry & Watson, 2007; Fu *et al.*, 2008). Five estimates for the value(s) of $aTiO_2$ have been proposed for the Bishop magma: 0.6, estimated by Watson *et al.* (2006) and Wark *et al.* (2007); 0.53 as calculated from Fe–Ti-oxide equilibrium modelling (Thomas *et al.*, 2010; Reid *et al.*, 2011); 0.15 using MELTS and 0.23 using rhyolite-MELTS (Thomas & Watson, 2012); and 0.45 – 0.67 calculated from Fe–Ti-oxide compositions by Ghiorso & Gualda (2013). An additional universal assumption is that the value of $aSiO_2$ is 1.0, based on the abundance of crystallising quartz in the Bishop Tuff.

Using the calibration of Ferry & Watson (2007), we calculated apparent temperatures (on 101 side-tip pairs) from measured Ti concentrations in the same growth zone. These calculations yield average apparent temperatures for the darker tips between 712 °C ($aTiO_2$= 0.67) and 863 °C ($aTiO_2$= 0.15) depending upon which value of $aTiO_2$ is used. In contrast the lighter sides yield average apparent temperatures of 686 °C ($aTiO_2$= 0.67) to 829 °C ($aTiO_2$= 0.15) (Electronic Appendix 3). This gives a range of apparent temperature difference of 20 – 50 °C for different sectors within the same crystal growth zone (Fig. 3.13a). If a constant T of 750 °C is assumed the difference in calculated $aTiO_2$ between the darker tips ($aTiO_2$= 0.44) and the lighter sides ($aTiO_2$= 0.34) is on average ~0.1. This difference in $aTiO_2$ increases at cooler temperatures, but is reduced at temperatures >750 °C.

Ti concentrations also vary between bright overgrowths and their respective cores (neither of which are visibly sector zoned in order for these variations to be estimated). The bright rims produce average apparent temperatures between 718 °C ($aTiO_2$ = 0.67) and 871 °C ($aTiO_2$ = 0.15) with an average range in apparent temperatures of 87 °C across all bright

rims. Cores yield apparent temperatures between 697 °C (aTiO$_2$ = 0.67) and 805 °C (aTiO$_2$ = 0.15) with an average range in apparent temperatures of 77 °C across the cores. The trend in Ti–U space of cores and rims are very different, both apparently evolving to (or from) a similar point (Fig. 3.13b). These calculated apparent temperatures for sectors and core-rim pairs are distinctly lower than those calculated using Fe–Ti-oxide thermometry (Hildreth, 1979; Hildreth & Wilson, 2007), two-pyroxene thermometry (Hildreth & Wilson, 2007) and Ti-in-quartz thermometry, when the same values of aTiO$_2$ are used (Wark *et al.*, 2007; Thomas *et al.*, 2010).

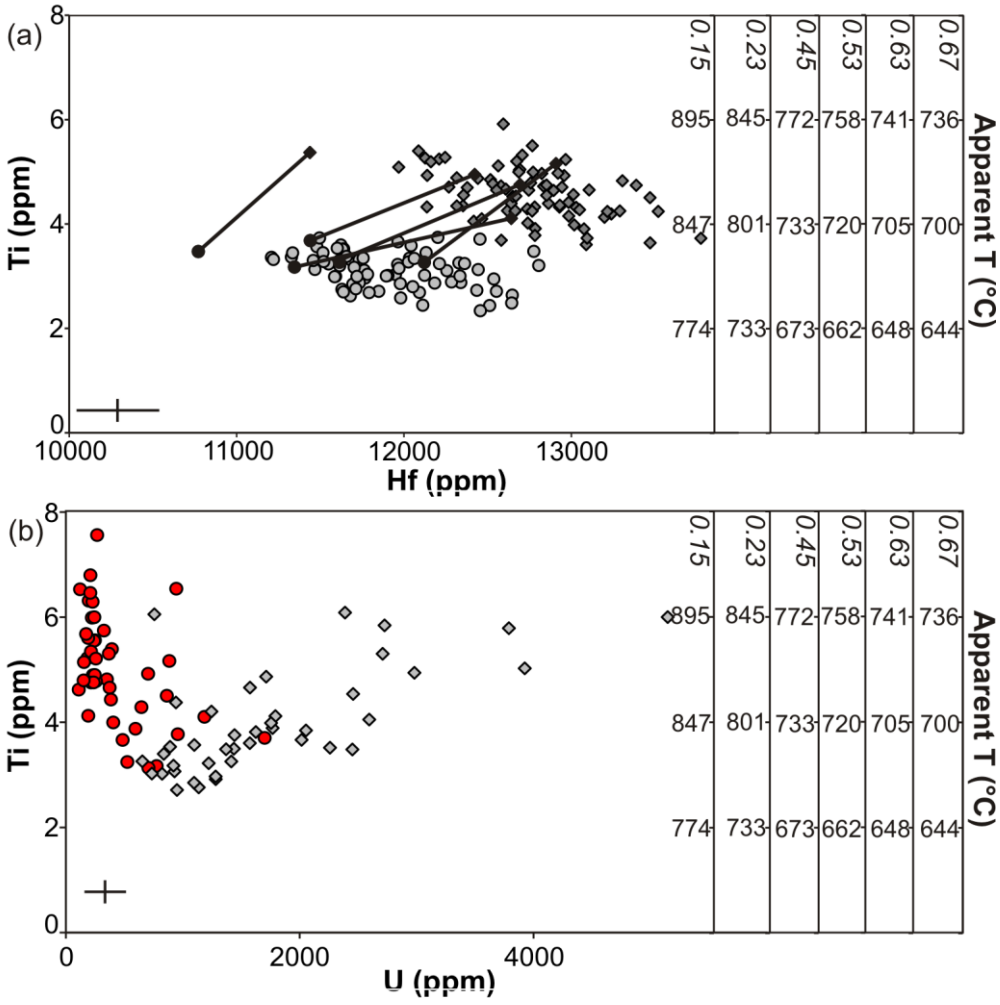

Fig. 3.13. Summary of results from Ti-in-zircon thermometry from Bishop zircons. (a) Comparisons of model temperatures obtained from Ti concentrations between different sectors of the same crystals: light grey circles are lighter sides, dark grey diamonds are darker tips. (b) Differences between CL-darker cores and CL-brighter rims of the same crystals: Red circles represent rims, grey squares represent cores. The *y*-axis is labelled with the measured Ti concentrations (ppm) on the left, and the resulting model temperature scales on the right based on the multiple published estimates of aTiO$_2$ (given in italics) proposed for the Bishop magma (see text for discussion). Cross represents 2σ uncertainty. (For full data set see Electronic Appendix 2.)

Considering Ti concentration alone, the Bishop zircons display a relatively limited range in Ti concentrations (2 – 8 ppm) when compared with other large silicic eruptives, such as the Oruanui (2 – 14 ppm), Ongatiti (3 – 18 ppm) and Kidnappers (2 – 18 ppm) examples in New Zealand (C. J. N. Wilson *et al.*, unpublished data). The nano-scale Ti variability reported by Hofmann *et al.* (2013), if generally present, would raise further issues over the measurement of Ti concentrations in zircon and interpretation of these values in terms of entry of Ti into the zircon structure (e.g. as nano-inclusions versus as a structural component) and consequent temperature estimates. However the great contrast in the sampling volumes of the NanoSIMS versus ion probe means that the two suites of data are not yet comparable.

3.5.2.3. Contributing components to the zircon population in the Bishop Tuff magma

By combining the textural, age and trace-element data sets it is clear that there are at least four components which have contributed to the zircon assemblages in the Bishop Tuff: (1) the magma that grew the sector-zoned 'normal Bishop' crystals, which are the dominant population in most of the Bishop samples examined (Table 3.2; Fig. 3.4); (2) the magma that caused the growth of bright rims (and sparse whole crystals) in the zircon population; (3) the xenocrystic crustal component, mostly from Triassic granitoids, and present at up to 20% of the zircon population in two samples (Table 3.2; Fig. 3.4); (4) the Glass Mountain component which dominates the YA dome sample, but forms only a minor component (6% maximum) of grains in the Bishop samples

The top of the magma chamber (sampled with F1 and Ig1Eb) is dominated by the normal Bishop zircons, rapidly grown (reflecting the sector zoning) and with no bright overgrowths. This situation highlights a lack of mixing within the upper parts of the magma chamber, consistent with the limited ranges in corresponding Bishop Tuff phenocryst and whole-rock compositions (Hildreth, 1979; Hildreth & Wilson, 2007). These early-erupted zircons have trace element variations dominated by sector zoning and ages close to eruption age (cores of F1 and Ig1Eb are dominantly aged from 760 to 820 ka). However, it is apparent from their relatively restricted Th/U ratios, only mildly affected by sector zoning (Fig. 3.10), that the source for the 'normal Bishop' zircons involved melting of an arc-sourced lithology (Miller & Wooden, 2004; Claiborne *et al.*, 2010). The trends evident in U vs Yb (Fig. 3.10) and most other element–element and element–ratio plots in which element concentrations are increasing with fractionation, are

likely to reflect continuing high-percentage fractionation of quartz and feldspar (up to 90% of the erupted crystal assemblage: Hildreth, 1979) which makes most of the trace elements common to zircon behave incompatibly in the melt. We cannot find evidence for allanite fractionation influencing zircon trace-element patterns, as there is no decrease in U and Th concentrations with increasing Hf (Fig. 3.10). Allanite fractionation has been proposed to explain a coupled decrease in light REE (LREE) and Zr/Hf in zircon (Reid *et al.*, 2011). Allanite is not present, however, in the late Bishop Tuff and the extremely low abundances of LREE in any zircons make monitoring LREE changes challenging.

With progression through the eruption sequence (i.e. deeper in the magma chamber) the zircon textures become more variable, with the magma responsible for the bright zircon rims first becoming present in significant amounts in the latest Ig1Eb deposits (Sherwin subunit). It had previously been thought that the bright rims on quartz and sanidine crystals (Hildreth, 1979; Anderson *et al.*, 2000; Peppard *et al.*, 2001; Wark *et al.*, 2007) were restricted to the northern units. Recent investigations of quartz-hosted melt inclusions have, however, revealed a more complex history (Roberge *et al.*, 2013). This study documented changes in melt inclusion compositions, from less evolved than the host melt, to more evolved than the host melt, taken as evidence of melt mixing occurring at depth within the magma chamber. This pattern of less evolved glass coupled with more evolved melt inclusions is not, however, restricted to the northern-erupted Bishop Tuff, but occurs also in the mid- to late-erupted eastern units (Ig2Ea, Ig2Eb). When coupled with the presence of the bright rims on zircons in late Ig1Eb, these observations imply that the introduction of a new magmatic component into the chamber caused growth of the zircon bright rims.

Samples from the later-erupted Bishop units (Ig2N, Ig2NW) contain a smaller proportion of sector-zoned zircons, with sparse crystals of Glass Mountain type (Table 3.2; Fig. 3.4). These contrasts suggest that zircon suites in the later-erupted units of the Bishop Tuff, inferred to come from deeper in the chamber (Wallace *et al.*, 1999), incorporate some influence from a longer-lived part of the magma system. Some minor inheritance from the Glass Mountain system is also inferred to be present on the basis of textural observations, although this is not reflected in the age spectra. If such grains are from a source common to the Glass Mountain system, then magmatism continued after eruption of the youngest Glass Mountain domes.

The later-erupted deeper-sourced magma, which contains zircons that began to crystallise at ~845 ka produced grains which do not show obvious sector zoning in CL, but are similar in trace element composition to those found in the early deposits (including some sectoral zoning in trace-elements such as P and Ti). Our data indicate that the melts from which the sector-zoned and non-sector-zoned zircons grew were broadly similar in composition and had experienced comparable degrees of fractionation. This cogenetic nature of the early versus late-erupted zircons is consistent with a unitary nature for the Bishop Tuff magma body (Hildreth, 1979; Hildreth & Wilson, 2007) and counts against any notion of two separate magma bodies (Gualda *et al.*, 2012a).

The trace to subordinate component of Triassic zircons, most abundant in the swirly pumice type (Hildreth & Wilson, 2007) indicates a late-stage incorporation of country-rock components into the magma (see also Hildreth, 1985). The Triassic zircons have a lower range in Th/U compared with the normal Bishop-type zircons (Fig. 3.10), indicating that melts of Triassic crust have not been a source for the main Bishop Tuff magma body. The lack of overgrowths on any of the zircon crystals implies that xenocrystic incorporation was very late-stage, most probably syn-eruptive.

3.5.3. Origin of the 'bright-rim' magma

Development of the CL-bright zircon rims is linked to changes in melt inclusion chemistry (Wallace *et al.*, 1999; Anderson *et al.*, 2000; Roberge *et al.*, 2013), and bright overgrowths found on quartz (CL imagery) and sanidine (BSE imagery) in the northern-erupted units (Anderson *et al.*, 2000; Peppard *et al.*, 2001; Morgan & Blake, 2006; Wark *et al.*, 2007; Gualda *et al.*, 2012b). It has been suggested that varying growth conditions (i.e. changes in T, P, fO_2) could have caused crystallisation of these bright rims on quartz, sanidine and zircon (Anderson *et al.*, 2000; Peppard *et al.*, 2001; Wark *et al.*, 2007; Thomas *et al.*, 2010). However, our trace-element data from bright rims show low concentrations of elements such as the HREE, U and Th compared with those of the sector-zoned zircons, indicating that these species were at lower concentrations within the parental melt. Using the partition coefficients of Sano *et al.* (2002) on the rims and cores of the same sectors indicates that the melt that crystallised the bright zircon was higher in Eu, but lower in the MREE and HREE than the melt associated with the sector-zoned zircons, assuming constant partition coefficients for both growth regimes. The difference between the bright rims and normal cores is more variable in Ig2Nb when compared with earlier-erupted units. This 'bright-

rim' melt had Th/U ratios of 0.3 – 0.6, similar to the normal Bishop sector zoned cores, which indicates that both the 'bright-rim' melt and the 'normal Bishop' melt involved the melting of a similar, arc-lithology source, consistent with the low U/Yb values of less than 1.0 (Fig. 3.10, Electronic Appendix 3). The lower values of HREE agree with previously published melt-inclusion and glass data (e.g. Anderson *et al.*, 2000; Roberge *et al.*, 2013), showing that these changes in the zircon trace elements match the evolution of host melt compositions. Increases in Ti concentration in the bright overgrowths yields ~20 °C higher apparent temperatures over the cores (independent of the value of $a\mathrm{TiO_2}$ used), possibly showing that the magma was hotter. This is in agreement with Fe–Ti-oxide thermometry, which shows that the eruption temperatures of the melts are higher in the later units (~815 °C versus ~715 °C; Hildreth & Wilson, 2007). However, owing to the highly incompatible nature of many key trace elements into zircon and the obvious overprinting from the sector zoning, more detail about the nature of this 'bright-rim' melt cannot be derived from zircon chemistry alone. Further investigations are currently under way to into the nature of the 'bright-rim' magma and its relationship to the minor less-evolved components in the Bishop Tuff (Hildreth, 1979; Hildreth & Wilson, 2007).

Introduction of the bright-rim forming magma has previously been considered to be on such a short timescale (<100 yrs) that it was a possible trigger for the Bishop Tuff eruption (Wark *et al.*, 2007). By calculating the weighted means of our age determinations from directly inside the bright rim it is apparent that these zones are systematically older than the true rim analyses (whether they are 'bright-rim' or 'normal'; Fig. 3.14). However, there is no linear relationship between the bright rim width and age inside the rim, so we cannot determine absolutely when the bright-rim magma started to invade the magma chamber, apart from that it must be within 10 kyr of eruption age, based on ages within the cores of crystals with wide bright rims (Fig. 3.14). There are therefore two possibilities for the timing of interaction with this 'bright-rim' melt. The first is that the systematic differences in rim width are due to a constant zircon growth rate, and therefore the increase in mean ages with bright-rim width (Fig. 3.14) shows that the 'bright-rim' magma was interacting with the roots of the Bishop system under the northern side of what became Long Valley caldera for a longer period of time. However, this is inconsistent with quartz diffusion timescales that indicate <100 years of interaction with the 'bright-rim' magma (Wark *et al.*, 2007; Gualda *et al.*, 2012b). The second possible interpretation of the differences in timescales with rim width is that it reflects a cessation of zircon growth (but no dissolution,

hence the euhedral core morphologies). Therefore, in the deepest parts of the magma chamber (where rims are typically thicker: see Fig. 3.4) the magma was close to (or just above) zircon saturation, and zircons had ceased growing until interaction with the 'bright-rim' magma triggered renewed growth. In the upper parts of the magma system, where bright rims on zircon are rare and thin, the magma remained zircon saturated (and therefore zircon continued to grow) until the shortly pre-eruptive interaction with the 'bright-rim' magma (Wark *et al.*, 2007).

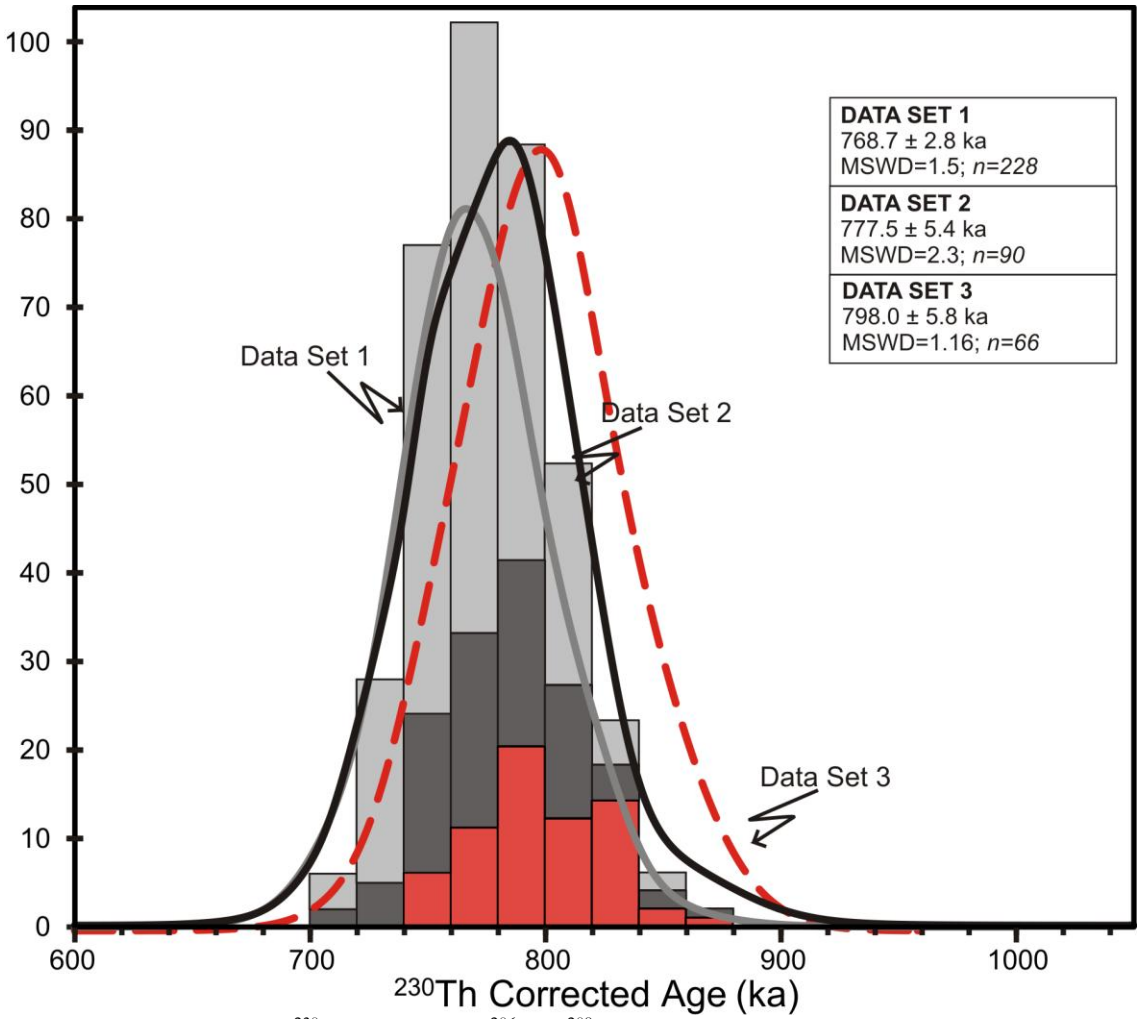

Fig. 3.14. Variation in ^{230}Th-corrected ^{206}Pb/^{208}U ages measured in 'normal Bishop' zircons (as defined from CL imagery; see text and Fig. 3.3). Data set 1 (light grey) combines all age determinations by us on rims of 'normal Bishop' zircons where there is no development of any CL-bright rim overgrowth. Data set 2 (dark grey) represents measurements on Bishop zircons which have narrow (<10 μm) bright rims, where the spots were sited in the darker CL cores just inside the brighter rim. Data set 3 (red, dashed line) represents measurements on Bishop zircons which have wide (>10 μm) bright rims, where the spots were sited in the darker CL cores just inside the brighter rim. Probability density function (PDF) curves from Isoplot. Values for the data sets represent the number of spots used (*n*), and the weighted means, uncertainties at 95% confidence and MSWD values for the respective populations. (For full data set see Electronic Appendix 1.)

To assess if introduction of the hotter 'bright-rim' magma would allow crystallisation of the observed bright rims, we calculated the state of zirconium saturation in the melt, using the Watson & Harrison (1983) calibration. In the samples dominated by 'normal' Bishop zircons the Zr saturation temperatures are within uncertainty of the published Fe–Ti-oxide and $\Delta^{18}O$ (Qz–Mt) temperatures, and therefore the melt was zirconium saturated, at least immediately prior to eruption (Hildreth, 1979; Bindeman & Valley, 2002). However, in the three samples which display high proportions of bright rims the Zr saturation temperatures are up to 50 °C lower than the Fe–Ti-oxide thermometry for those units, implying that the 'bright-rim' melt was slightly Zr undersaturated. This result would seem to indicate that the 'bright-rims' must have grown before those modelled in quartz. However, Harrison *et al.* (2007) propose that zircon can crystallise at up to 80 °C higher than the zircon saturation temperature calculated from Watson & Harrison (1983). In addition, it is unlikely that the zircon bright-rims are unrelated to the bright rims observed in quartz and sanidine, given the similar associated trace element changes (Hildreth, 1979; Anderson *et al.*, 2000; Wark *et al.*, 2007; Simakin & Bindeman, 2008).

3.6. Conclusions

This study demonstrates some key findings that are not only relevant to the development and eruption of the Bishop Tuff magma body, but that also raise important considerations for zircon studies on any silicic system.

1. A comprehensive suite of U–Pb ages from the earliest to the latest units of the Bishop Tuff reveal no evidence for a long 'tail' to the precursory Glass Mountain system, and we cannot replicate published peaks in age spectra greater than ~845 ka. Our nearest-rim analyses in samples from early erupted material yield a weighted-mean estimate for the eruption age of 766.6 ± 3.1 ka (95% confidence), fully consistent with the ID-TIMS estimate of Crowley *et al.* (2007) and $^{40}Ar/^{39}Ar$ age determinations of Rivera *et al.* (2011). Our data are not consistent with proposals of older ages for the Fish Canyon standard that would have the Bishop eruption age in the 776-778 ka range (Renne *et al.*, 2010, 2011; Mark *et al.*, 2012). SIMS chronologies on zircons, at least in this key example, can match in overall accuracy and precision those obtained by ID-TIMS, with the advantage of being able to link analytical spot positions to textural features within grains.

2. Zircon age data from the youngest Glass Mountain dome (YA) are consistent with an eruption age of 862 ± 23 ka, in contrast to the universally used K-Ar value of 790 ± 20 ka (Metz & Mahood, 1985). Our data, coupled with zircon ages and $^{40}Ar/^{39}Ar$ age determinations from Glass Mountain dome OD (Davies *et al.*, 1994; Simon & Reid, 2005) imply that the K-Ar chronological framework of Metz & Mahood (1985) may be significantly inaccurate.

3. Our age data show that the Bishop Tuff magma and mush systems were physically separated from the Glass Mountain system and must have evolved in separate fashion. Textural data imply that there was very little (<10%) zircon crystal inheritance from the Glass Mountain roots even in the deepest parts of the magma chamber. Our ages imply that the Bishop magma system began its operations with zircon saturated compositions only to begin crystallising zircon ~80 kyr prior to eruption. This is not necessarily the assembly time for the melt-dominant magma body, but the lack of systematic textural contrasts between zircons spanning this ~80 kyr range suggests that this was the case.

4. The Bishop zircons can be classified into four categories: (a) a numerically dominant suite of sector zoned grains; (b) a subordinate suite of grains with rims of CL-bright material (and cores that may or may not show sector zoning); (c) a sparse suite of grains with oscillatory zoning and shapes that match the dominant population in Glass Mountain dome YA; and (d) oscillatory zoned Mesozoic crustal xenocrysts. We demonstrate that a major control on trace-element variations in the Bishop zircon population is imposed by sector zoning. This sector zoning is most dominant in crystals from the early Bishop Tuff units which are representative of the archetypical and numerically dominant 'normal Bishop' type of zircon. Application of Ti-in-zircon model temperatures in particular is hindered both by the sector zoning (differences of 20 – 50 °C between sides and tips in the same growth zone in the same crystals) and by contrasting values proposed for the value of $a TiO_2$ (0.15 – 0.67).

5. Despite the strong influence of sector zoning, key magmatic features can still be identified. By combining textural observations from CL imagery and trace-element analyses, two major end-member host magmas for the Bishop Tuff are identified, one responsible for the 'normal Bishop' sector-zoned zircons and the other responsible for the CL-bright components. The 'bright-rim' component was a less evolved late-stage

contributor to the Bishop system, and it also influenced growth of bright rims on sanidine and quartz. However, 'rejuvenation' of the Bishop magma chamber is observed to reach levels as shallow as those tapped by the latest Ig1Eb unit, earlier than has been previously identified. The sources for the Bishop Tuff magmas (whether 'normal' or that responsible for the bright-rims) appear to involve an evolved arc source, which subsequently experienced significant proportions of quartz and feldspar fractionation.